

Diffusion mechanism and electrochemical investigation of 1T phase Al-MoS₂@rGO nano-composite as a high-performance anode for sodium-ion batteries

Manish Kr. Singh,^{1,*} Jayashree Pati,^{1,*} Deepak Seth,² Jagdees Prasad,¹ Manish Agarwal,³ M. Ali Haider,² Jeng-Kuei Chang,⁴ and Rajendra S. Dhaka^{1,†}

¹*Department of Physics, Indian Institute of Technology Delhi, Hauz Khas, New Delhi-110016, India*

²*Renewable Energy and Chemicals Group, Department of Chemical Engineering, Indian Institute of Technology Delhi, Hauz Khas, New Delhi-110016, India*

³*Computer Service Center, Indian Institute of Technology Delhi, Hauz Khas, New Delhi- 110016 India*

⁴*Department of Materials Science and Engineering, National Yang Ming Chiao Tung University, Hsinchu 30010 Taiwan*

(Dated: October 14, 2022)

We report the electrochemical investigation of 5% Al doped MoS₂@rGO composite as a high-performance anode for sodium (Na)-ion batteries. The x-ray diffraction (XRD), Raman spectroscopy and high-resolution transmission electron microscopy characterizations reveal that the Al doping increase the interlayer spacing of (002) plane of MoS₂ nanosheets and form a stable 1T phase. The galvanostatic charge-discharge measurements show the specific capacity stable around 450, 400, 350, 300 and 200 mAhg⁻¹ at current densities of 0.05, 0.1, 0.3, 0.5 and 1 Ag⁻¹, respectively. Also, we observe the capacity retentions of 86% and 66% at 0.1 and 0.3 Ag⁻¹, respectively, over 200 cycles with a consistent Coulombic efficiency of nearly 100%. The cyclic voltammetry, galvanostatic intermittent titration technique, and electrochemical impedance spectroscopy are used to find the kinetic behavior and the obtained value of diffusion coefficient falls in the range of 10⁻¹⁰ to 10⁻¹² cm²s⁻¹. Intriguingly, the *in-situ* EIS also explains the electrochemical kinetics of the electrode at different charge-discharge states with the variation of charge transfer resistance. Moreover, the post cycling investigation using *ex-situ* XRD and photoemission spectroscopy indicate the coexistence of 1T/2H phase and field-emission scanning electron microscopy confirm the stable morphology after 500 cycles. Also, the Na-ion transport properties are calculated for 1T Al-MoS₂@rGO interface and Al-MoS₂-MoS₂ interlayer host structure by theoretical calculations using density functional theory. **Key words:** sodium-ion batteries; anode materials; Al-MoS₂@rGO; electrochemical performance.

I. INTRODUCTION

The gradual depletion of fossil fuels and emission of greenhouse gases due to their combustion, pave the way toward renewable energy resources like solar and wind [1–3]. However, the conversion of energy through these resources depend on several environmental factors and not ample to meet the energy demands when required. Therefore, the present research is geared towards energy

storage and conversion devices for the restoration of renewable energy. As we know, the lithium-ion batteries (LIBs) are one of the most efficient technology among various energy storage devices on the subject of energy density and power density [4–6]. The LIBs are virtually the heart of all portable devices such as laptops, mobiles, as well as the electric vehicles [7–10]. However, due to the increasing demand with time, and the uneven geographical and limited distribution of lithium across the world, the LIBs are becoming more expansive and not affordable for common society [11, 12]. In this context, sodium being widely and evenly distributed throughout as well

* These authors contributed equally to this work

† rsdhaka@physics.iitd.ac.in

as its similar electrochemistry make the sodium-ion batteries (SIBs) potential candidates for cost-effective and complementing the LIBs [13, 14]. However, it is not that easy as there are great challenges, mainly coming from the larger size of sodium (1.02 Å), which need to be resolved in order to design efficient electrode materials with appealing characteristics for energy storage applications [15–18]. Among the bottlenecks, searching the anode materials with high capacity, better rate capability, and excellent cycle life are major challenges, because graphite cannot be used due to its reactivity/thermodynamic instability with sodium [19, 20].

At present, the SIB anode materials based on alloying and conversion are widely used because of their high theoretical capacity [21, 22]. On the other hand, the insertion based materials provide excellent cycle life, but with a low specific capacity in SIBs [23]. The sodium-ion uptake is limited for insertion based compounds due to their rigid frameworks [24]. However, the metals and metalloids based materials have the ability of multiple sodium-ion uptakes per single atom resulting in capacities ranging from 300 to 2000 mAhg⁻¹ with operational voltages below 1 V vs Na/Na⁺ as anode in SIBs. Mostly, group-15 (pnictogen), group-16 (chalcogen), and transition metals are used for the production of alloying and conversion based complexes [14]. Among these, the transition metal dichalcogenides (TMDs) and particularly sulfides are of much importance because of their low cost, high capacity, and environment friendly nature. Furthermore, the low activation energy between transition metal and sulfur in TMDs facilitates the Na-ion migration during charging-discharging, while its high theoretical capacity offers high energy density for SIBs [25]. Particularly, the molybdenum disulfide (MoS₂) with a two-dimensional open framework has attracted considerable attention among TMDs due to its structural flexibility and high theoretical capacity as an anode material for both LIBs and SIBs [26] as well as Zn-ion batteries [27, 28]. The MoS₂ is found in three phases namely 1T, 2H, and 3R where the 1T phase

shows metallic nature with better ion and electron transport as compared to 3R and 2H phases because of two reasons [29–36]: (i) it has a distorted octahedral coordination structure which results in high electronic conductivity as compared to 2H and 3R phases, (ii) another advantage is its high hydrophilic nature which enables affinity of electrolytes [37, 38]. In addition to these factors, its revealing electrochemical active sites and large inter-layer spacing (0.93 nm) with wide and fast ion-diffusion channels make the 1T phase more suitable for Na⁺ ion storage [33].

In this line, one of the most effective ways to enhance the electrochemical activity of MoS₂ as an anode in SIBs, is to fabricate nano-composite of MoS₂ particles through different synthesis routes to minimize the diffusion length of Na-ion during sodiation/de-sodiation [39, 40]. Chen *et al.* developed a scalable chemical vapor deposition method to prepare MoS₂ deposited electrospun carbon nanofiber hybrid to enhance the ionic conductivity, that provides large contact area for electrolyte and prevent the MoS₂ nanosheets agglomeration. This anode material exhibited a reversible capacity of 198 mAhg⁻¹ after 500 cycles at a current density of 1 Ag⁻¹ [41]. In order to study the effect of conductive carbon matrices, Sahu *et al.* synthesized modified 3-D framework of MoS₂@rGO hybrid through hydrothermal route, which was observed to deliver high discharge capacities of 588 mAhg⁻¹ and 501 mAhg⁻¹ at current densities of 100 and 500 mA g⁻¹ with capacity retention of 98% and 92.3% after 80 and 250 cycles, respectively [42]. Here, the rGO nano-sheets act as backbone to hold the MoS₂ nano-plates during cracking of the material owing to its high surface area and mechanical strength [42]. Also, one way to enhance the electronic conductivity and to adhere the volume expansion, is to modify MoS₂ with different conductive carbon matrices like rGO, CNT, carbon-doped with nitrogen and sulfur, etc. Additionally, the hetero-atom doping is also another efficient approach for improved structural stability and boosting volume expansion in MoS₂ [36, 43, 44].

Li *et al.* proposed the improved cycling stability of Co-doped 1T MoS₂ than the pristine MoS₂, where the introduction of Co mitigates the volume expansion up to 52% during cycling [34]. Interestingly, a moderate Sn-doped 1T-2H MoS₂ anode was reported by Zeng *et al.*, which provides a significant rate capability of 167 mAhg⁻¹ at a current rate of 15 Ag⁻¹ with cycling retention of 320 mAhg⁻¹ after 500 cycles at 1 Ag⁻¹ [45]. Moreover, using first-principles calculations the sodium-ion intercalation and diffusion mechanism are reported in different phases of MoS₂/graphene layer [46].

Here, we have synthesized MoS₂, MoS₂@rGO, CNT-MoS₂@rGO, and 5% Al doped MoS₂@rGO composites by a simple hydrothermal method. We found that the doping of Al ions enhance the interlayer spacing of (002) crystal plane of pure MoS₂@rGO nano-sheets and stabilize in a stable 1T phase, as confirmed by x-ray diffraction (XRD), Raman spectroscopy and transmission electron microscopy (TEM) measurements. Interestingly, we observe significant enhancement in the electrochemical performance of Al doped MoS₂@rGO, which exhibits the discharge specific capacity of around 400 mAhg⁻¹ at a current density of 100 mA g⁻¹, which found to be highly stable for more than 200 cycles even at faster charge-discharge rates with about 100% Coulombic efficiency. The diffusive behavior in the electrode material is also investigated through detailed analysis of CV, EIS, and GITT data, and the diffusion coefficient was found to be in the range of 10⁻¹⁰ to 10⁻¹² cm²s⁻¹. The post-cycling analysis performed after 500 cycles at a current density of 500 mA g⁻¹ through room temperature XRD and FE-SEM measurements confirm the structural evolution and morphological stability of the anode material. The photoemission results indicate the 1T phase of pristine sample and coexistence of 1T/2H hetero-structure phase for the cycled anode material. We have also employed density functional theory to understand the Na-ion migration in the inter-layered structures of 1T phase Al-MoS₂@rGO.

II. METHODS

2.1.1 Synthesis of graphite oxide (GO): The GO nano-sheets were synthesized by chemical oxidation of bulk graphite powder using a slightly modified Staudenmaier process [47]. In this typical procedure, 180 ml of concentrated H₂SO₄ was gradually combined with 90 ml of HNO₃ in a 500 ml beaker while stirring with an ice bath. We added 10 gms of graphite powder slowly into the prepared solution with continuous stirring for 30 minutes. Then, 110 gms of KClO₃ was added for an extended time of 2-2.5 hrs. The ice bath was withdrawn, and the solution was left to stir at ambient temperature for the next 5 days. The obtained GO solution was first washed 7-8 times with DI water and then with 10% solution of hydrochloric acid to remove (SO₄)²⁻ ions and other impurities. The resulting material was centrifuged 6-7 times in purified DI water. The obtained GO powder was finally vacuum dried overnight at 80 °C.

2.1.2 Synthesis of MoS₂, MoS₂@rGO, CNT-MoS₂@rGO: The pure MoS₂, composite of MoS₂@rGO and CNT-MoS₂@rGO were prepared by a simple one step hydrothermal method. For the preparation of pure MoS₂ nano-sheets, 30 mmol of thiourea [(NH₂)₂CS] and 1 mmol of ammonium molybdate tetrahydrate [(NH₄)₆Mo₇O₂₄·4H₂O] were homogeneously dispersed for 1 hr under the constant magnetic stirring in 40 ml of DI water. The obtained black colored homogeneous solution was transferred into a 100 mL Teflon-lined stainless steel autoclave and heated at a constant temperature of 220°C for 24 hrs. It was followed by cooling the system to room temperature naturally so that the obtained black powder can be washed with absolute ethanol and DI water several times. Then, the obtained precipitate was dried in a vacuum oven at 65°C for 12 hrs and the resultant powder of MoS₂ was obtained. For the synthesis of MoS₂@rGO and CNT-MoS₂@rGO composites, we use 140 mg of GO powder and 100 mg of CNT, which were dispersed homogeneously in 40 ml of DI water with the

help of sonication for 1.5 hrs. After that, all the other steps were similar to the formation of pure MoS₂.

2.1.3 Synthesis of Al-doped MoS₂@rGO: The Al-MoS₂@rGO nano-hybrids were synthesized using a facile hydrothermal method. First we mix 140 mg (3.5 mg/mL) of GO powder and 12.70 mg of AlCl₃·6H₂O in 40 mL DI water under steady ultra-sonication for 2 hrs at room temperature to make a homogenous suspended solution. After that, 30 mmol (NH₂)₂CS and 1 mmol (NH₄)₆Mo₇O₂₄·4H₂O were slowly added to the above formed suspension along with constant stirring for 1 hr. A homogenous dark black solution was obtained, which then placed into a Teflon-lined stainless-steel autoclave (100 mL). A box furnace was used to heat the autoclave at 220 °C for 24 hrs, and then cooled to room temperature when the reaction time was completed. To remove the residual ions, the obtained black precipitate was centrifuged at 3000 rpm for at least 4-5 times using DI water and absolute ethanol. Finally, a black powder of Al-MoS₂@rGO was obtained by drying the washed product in a vacuum oven at 65 °C for 12 hrs.

2.2 Structural and physical characterizations:

To investigate the crystallographic structure of the active material, we perform the x-ray diffraction (XRD) measurements (Panalytical Xpert 3) with CuK α radiation (1.5406Å) in 2θ range of 5° to 80°. We use high-resolution transmission electron microscopy (HR-TEM) with a Tecnai G2-20 system, and field emission scanning electron microscope (FE-SEM) and energy dispersive x-ray (EDX) using the Quanta 200 FEG system to study the morphology, structure, elemental composition, and the distribution of elements across the sample. The Raman spectra were recorded with 532 nm wavelength laser using a Renishaw inVia confocal microscope having 2400 lines/mm grating and 10mW power on the sample. The x-ray photoelectron spectroscopy (XPS) with Al K α source (1486.6 eV), from Thermo Fisher Scientific, was used to investigate the core-level binding energy (BE) of different elements present in the sample before and after

cycling.

2.3 Coin-cell fabrication: The uniform slurry was prepared by taking 5%Al-MoS₂@rGO as an active material, CNT as conductive carbon, and polyvinylchloride (PVDF) binder in N-methylpyrrolidone (NMP) solvent in a weight ratio of 8:1:1. The slurry was then coated on a copper foil using a doctor blade method with active material mass loading about 1 mg cm⁻² followed by vacuum drying at 120 °C overnight to evaporate the excess solvent and moisture. The electrodes were cut and dried in vacuum before inserting them into the glove box (Uni-Lab Pro SP from MBraun). The CR2032 coin cells were fabricated in Ar filled glove box under a controlled level of O₂ and H₂O (less than 0.1 ppm). The Na foil was used as the counter and reference electrode. The electrolyte used was 1 M NaPF₆ in a mixture of ethylene carbonate (EC) and diethyl carbonate (DEC) 1:1 (vol %) with 5 wt % fluoroethylene carbonate (FEC) .

2.4 Electrochemical measurements: The galvanostatic charge-discharge (GCD) profiles were obtained by using a Neware battery analyzer BTS400 in voltage window 0.005–2.5 V (vs Na⁺/Na) at different current densities. The cyclic voltammetry (CV) was conducted at different scan rates using a Biologic VMP-3 model in the same voltage range as in GCD measurements. The electrochemical impedance spectroscopy (EIS) measurements were performed using a Biologic VMP-3 model in the frequency range of 10 mHz to 100 kHz, and the *ac* voltage amplitude was set to 10 mV at the open circuit voltage (OCV) state of the cells.

2.5 Theoretical calculations:

A model MoS₂@rGO interface is constructed with a monolayer of MoS₂ in a supercell size of 5×4×1 and 20 formula units, which are stacked with a 5×5×1 supercell of rGO layer. On geometry optimization of the structure, a sodium atom was introduced at one of the stable sites. Similarly, 5% Al doped MoS₂-MoS₂ interlayer structure is constructed. The transport of sodium-ion in these host materials interlayer is simulated using plane wave basis

set code of DFT as implemented in vienna *ab initio* simulation package (VASP-6.2) [48]. A plane wave cut-off energy of 500 eV is considered for the basis set expansion. The electron-ion core interactions are described by gradient-corrected projector augmented wave (PAW) [49] pseudo potential using Perdew-Burke-Ernzerhof (PBE) exchange-correlation functional [50], to solve the Kohn-Sham equations, which estimate the ground state energy of the structures. A $2 \times 2 \times 2$ gamma-centred k-point mesh is used for Brillouin zone integration. The convergence criteria for energy and force are kept at 10^{-6} eV and 0.05 eV/Å, respectively, for structural optimization using the conjugate gradient algorithm. To determine the minimum energy path (MEP) for sodium-ion migration and calculation of energy barriers, the CI-NEB (climbing image nudged elastic band) method is implemented [51, 52]. The optimized structure of Na-Al-MoS₂@rGO is taken as the initial state (IS) and corresponding structure after sodium-ion migration to the next available site is taken as the final state (FS) respectively, for transition state (TS) calculations. We use eight linearly interpolated images along the MEP between IS and FS. The convergence criteria considered for TS calculations are 10^{-5} eV and 0.05 eV/Å for energy and forces respectively. The activation energy (E_{act}) for sodium-ion migration is calculated as the difference in energy of the TS and IS.

III. RESULTS AND DISCUSSION

3.1 Structural/morphological characterization:

First the crystal structure of as prepared MoS₂, MoS₂@rGO, CNT-MoS₂@rGO, and Al-MoS₂@rGO composites is investigated using the XRD measurements at room temperature. The diffraction patterns of MoS₂, MoS₂@rGO and CNT-MoS₂@rGO are appeared to be very similar to each other having four major peaks located at about $2\theta = 14.14^\circ$, 33.30° , 39.34° , and 59.06° , which are indexed to the lattice planes (002), (100), (103), and (110) of the crystalline 2H phase of MoS₂,

respectively [Fig. 1(a)]. The peak corresponding to (002) with an interlayer spacing of about 6.3 Å signifies the crystalline multilayers of pure MoS₂ with hexagonal phase and the peak (100) depicts the stacking of Mo-S edges in vertical planes as well as the number of S active ions in the edge, as shown in Fig. 1(a). More importantly, the Al-MoS₂@rGO composite exhibits a new second order diffraction peak (004) located at about $2\theta = 17.06^\circ$ and the (002) peaks shifted to lower $2\theta = 9.1^\circ$ value where the calculated d spacing found to be 5.2 and 9.3 Å, respectively. This confirms the transformation from 2H phase to 1T phase with Al doping in MoS₂@rGO composite. This new phase has an increased interlayer spacing upon the intercalation of Al and NH₃/NH₄⁺ ions released as by-products of thiourea used as a reductant in the hydrothermal reaction [53–55]. Notably, the negatively charged surface of GO inhibits the approaching process of MoO₄²⁻ precursors, which prevents the nucleation of MoS₂ with proper spacing between interlayers [42]. However, in the present case of Al doped MoS₂@rGO, the modification through Al³⁺ dopant increases the electrostatic interaction between MoO₄²⁻ and negatively charged GO surfaces. This phenomenon accelerates the MoS₂ nucleation and provides large space for NH₄⁺ ions occupation at the proper sites, which increases the interlayer distance along (002) direction [56]. For example, the presence of NH₄⁺ ions between the layers is evident from the increment in the interlayer distance by about $\Delta d = 3$ Å, which is comparable to the size of NH₄⁺ ions (3.75 Å) [56]. Additionally, no peaks corresponding to any impurity were detected, which further indicating the phase purity of the composites. We successfully prepared 1T phase by doping 5% Al in MoS₂@rGO composite having $d = 9.3$ Å, which is considered to be a potential anode for sodium-ion batteries [57, 58]. The Raman measurement are performed to further explore the structure of all these samples, as shown in Fig. 1(b). The spectra of MoS₂, MoS₂@rGO, and CNT-MoS₂@rGO display intense E_{2g} and A_{1g} peaks at about 380 and 405

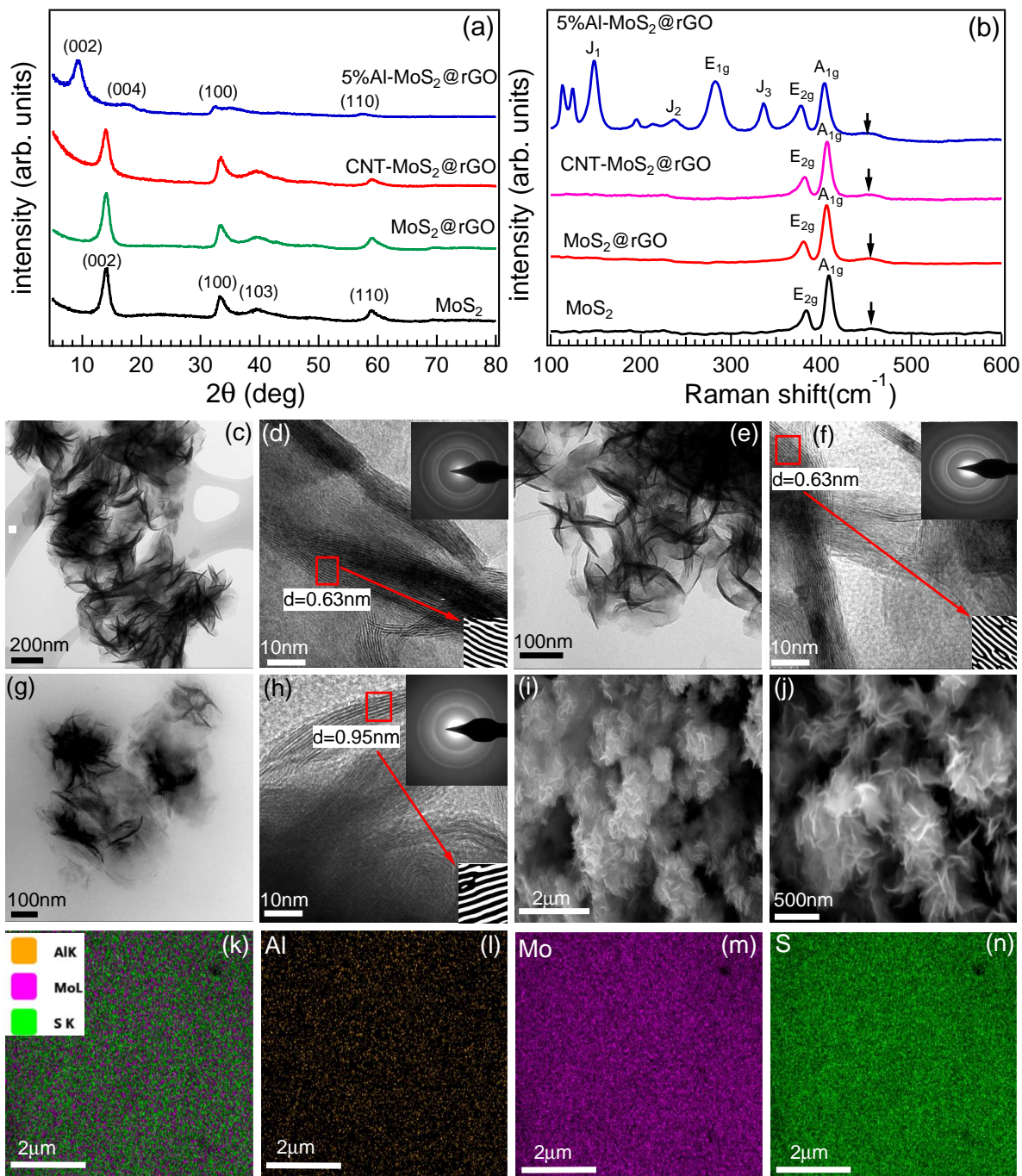


FIG. 1. (a) The XRD patterns and (b) the Raman spectra of MoS₂, MoS₂@rGO, CNT-MoS₂@rGO and Al-MoS₂@rGO measured at room temperature. The HR-TEM images of MoS₂@rGO (c, d), CNT-MoS₂@rGO (e, f), and Al-MoS₂@rGO (g, h) with the respective SAED patterns and the magnified views in the insets of (d, f, h). The FE-SEM images in (i, j), and the EDX mapping of Al, Mo and S in (k-n) for the Al-MoS₂@rGO composite.

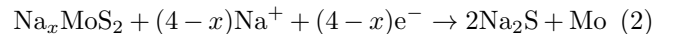
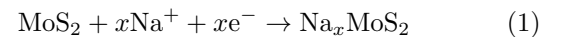
cm^{-1} , respectively, corresponding to in-plane and out of plane vibration of S–Mo–S and peak at around 455 cm^{-1} is correspond to longitudinal acoustic phonon mode [59]. In case of the Al–MoS₂@rGO, the E_{2g}, A_{1g} and peak corresponds to longitudinal acoustic phonon mode are obtained at around 377, 403 and 453.5 cm^{-1} , respectively. Interestingly, the specific phonon modes J₁ (147.8 cm^{-1}), J₂ (237 cm^{-1}) and J₃ (335.7 cm^{-1}) of Al–MoS₂@rGO corresponds to the formation of superlattice structure and symbolized as the characteristic peaks of metallic 1T phase. Further, the broadening and weak intensity ratio of A_{1g} to E_{2g} modes also suggest for the 1T phase due to the intercalated cations as well as that the Mo is coordinated octahedrally in 1T phase [60]. The XRD and Raman studies demonstrate that the Al doping drives the stabilization of 1T phase in MoS₂@rGO composite. Also, the defects due to disorder graphitic structures are determined for these composites taking the intensity ratio of D and G bands observed in the Raman spectra, as shown in Fig. 1 of [61].

Figs. 1(c-j) show the high-resolution TEM and FE-SEM images to analyze the microscopic structure and the morphology of all the samples, MoS₂@rGO, CNT-MoS₂@rGO, and Al–MoS₂@rGO, respectively. In Fig. 1(c), the flowery architecture is clearly visible due to the 3-D interconnected MoS₂@rGO nano-sheets, whereas the CNT wrapped MoS₂ flakes are shown in the Fig. 1(e). These nano architectures flower like morphology show porous structures, where rGO nano-sheets are intercalated into MoS₂ forming nano petals. The flexible and porous rGO nano-sheets increase the electronic conductivity and active surface area of the MoS₂ composites due to the 3-D interconnected paths. The HR-TEM images in Figs. 1(d, f, h) display some ripples in the nano-sheets with few folded edges of MoS₂, which can be seen as the dark contrast objects well dispersed over a grey background of rGO nano-sheets. The curled edges also reveal the lattice fringes having an inter-planar spacing of 6.3 \AA , 6.3 \AA and 9.5 \AA corresponding to (002) crystal planes

of the 2H phase of MoS₂@rGO and CNT-MoS₂@rGO, and 1T phase of Al–MoS₂@rGO, respectively, which are found to be consistent with the XRD patterns. The SAED patterns in the insets of Figs. 1(d, f, h) display hazy and broad diffraction rings. The porous nano architectures flowery like structure of Al–MoS₂@rGO composite with its relatively large interlayer distance provides a significant charge-storage capacity by facilitating a large number of Na-ion intercalation and also enhances the stability owing to the higher mechanical strength of rGO nano-sheets [62]. The FE-SEM images in Figs. 1(i, j) are also conforming the flower like morphology of Al–MoS₂@rGO composite. In Figs. 1(k-n), the elemental mapping images of Al–MoS₂@rGO confirm the uniform distribution of Al, Mo and S elements. The thermogravimetric analysis (TGA) confirms around 7wt% of the rGO content in the sample, as shown in Fig. 2 of [61].

3.2 Cyclic voltammetry (CV) and galvanostatic charge-discharge (GCD) investigation:

In order to demonstrate the redox mechanism during sodium ion intercalation in 1T Al–MoS₂@rGO host electrode, the CV measurement are performed at a scan rate of 0.05 mVs^{-1} in the voltage window of 0.005–2.5 V. Fig. 2(a) displays first few cycles of CV profile, which depicts three reduction (cathodic) peaks/shoulders at 1.1, 0.66 and 0.005 V and three corresponding oxidation (anodic) peaks at 1, 1.8 and 2.2 V. The first cathodic peak at 1.1 V involves the formation of Na_xMoS₂ due to the Na-ion insertion into the MoS₂ host structure as well as the SEI formation [43, 63], whereas the peak at 0.66 V is assigned to the conversion of Na_x MoS₂ resulting disintegration of MoS₂ into Mo particles embedding in Na₂S matrix [64], see for example below equations:



Additionally, the third sharp cathodic peak at 0.005 V indicates the intercalation of Na-ion between Na₂S and Mo

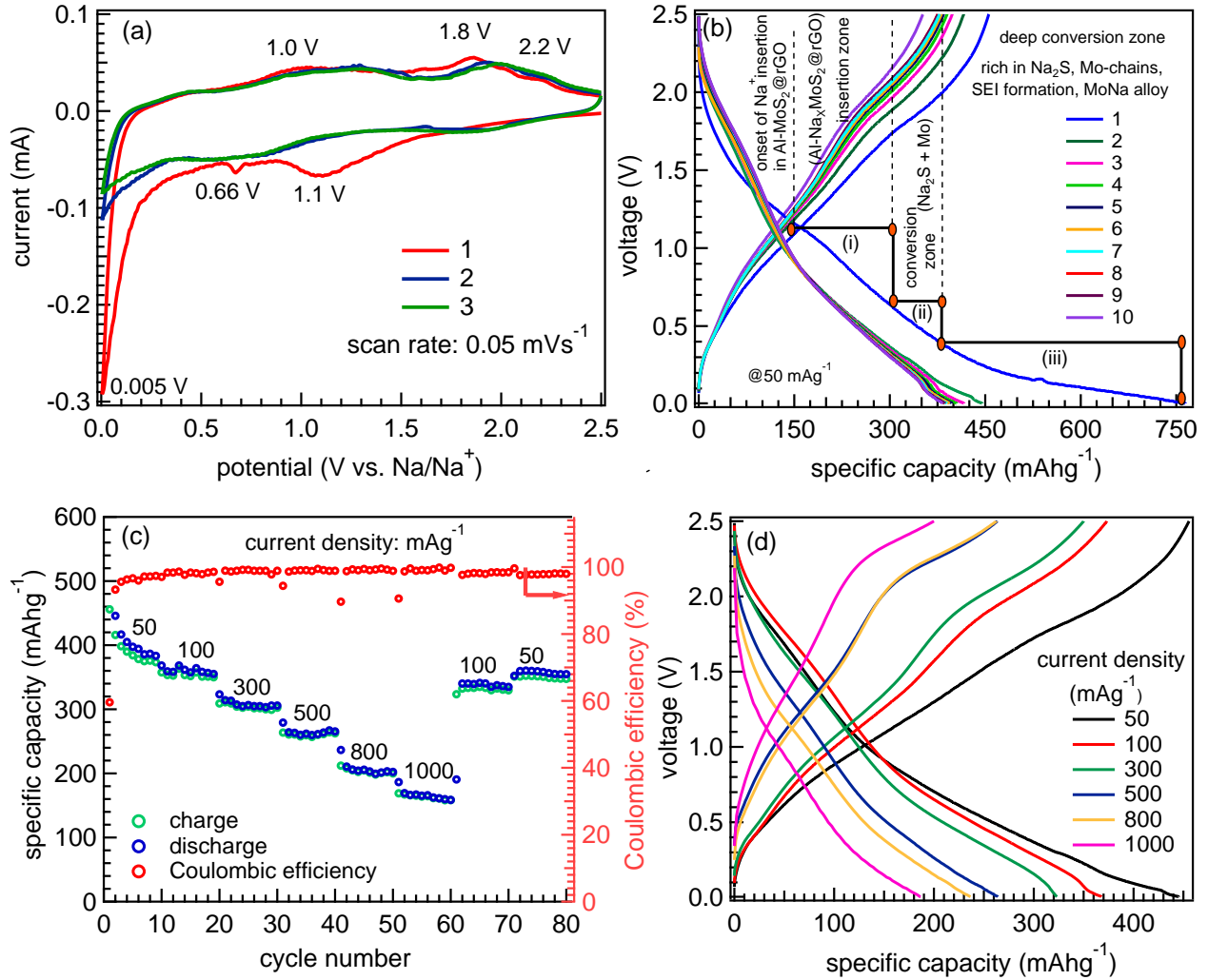


FIG. 2. The electrochemical measurements of Al-MoS₂@rGO electrode: (a) the cyclic voltammetry curves at a scan rate of 0.05 mVs⁻¹ for first 3 cycles in a voltage window of 0.005–2.5 V, (b) the GCD profiles at 50 mA g⁻¹ for the first 10 cycles, (c) the rate capability test with the Coulombic efficiency, and (d) the second cycle GCD profiles at each current density.

interface [35]. The oxidation peak at 1.8 V is attributed to the reverse reaction of metallic Mo nano-grains and Na₂S as described below [42]:



whereas, a small anodic peak at 2.2 V represents the oxidation of Na₂S to S or polysulfide [65]. The subsequent CV curves of 1T Al-MoS₂@rGO anode are almost overlapped after the 1st cycle, implying a reversible sodiation/desodiation process and electrochemical stability.

Fig. 2(b) shows the galvanostatic charge-discharge

(GCD) curves in the voltage window of 0.005–2.5 V for first 10 cycles at current density of 50 mA g⁻¹. The GCD curves show sloping features in the initial cycle and gradually inconspicuous plateaus are observed in the subsequent cycles during sodiation process. Notably, three plateaus are clearly visible in the initial sodiation process, which are consistent with the CV scans, where the first plateau located around 1.1 V denotes the insertion of Na-ions into the interlayers of MoS₂ (as discussed in equation 1), whereas the second plateau originates at 0.6 V corresponds to the conversion reaction involving

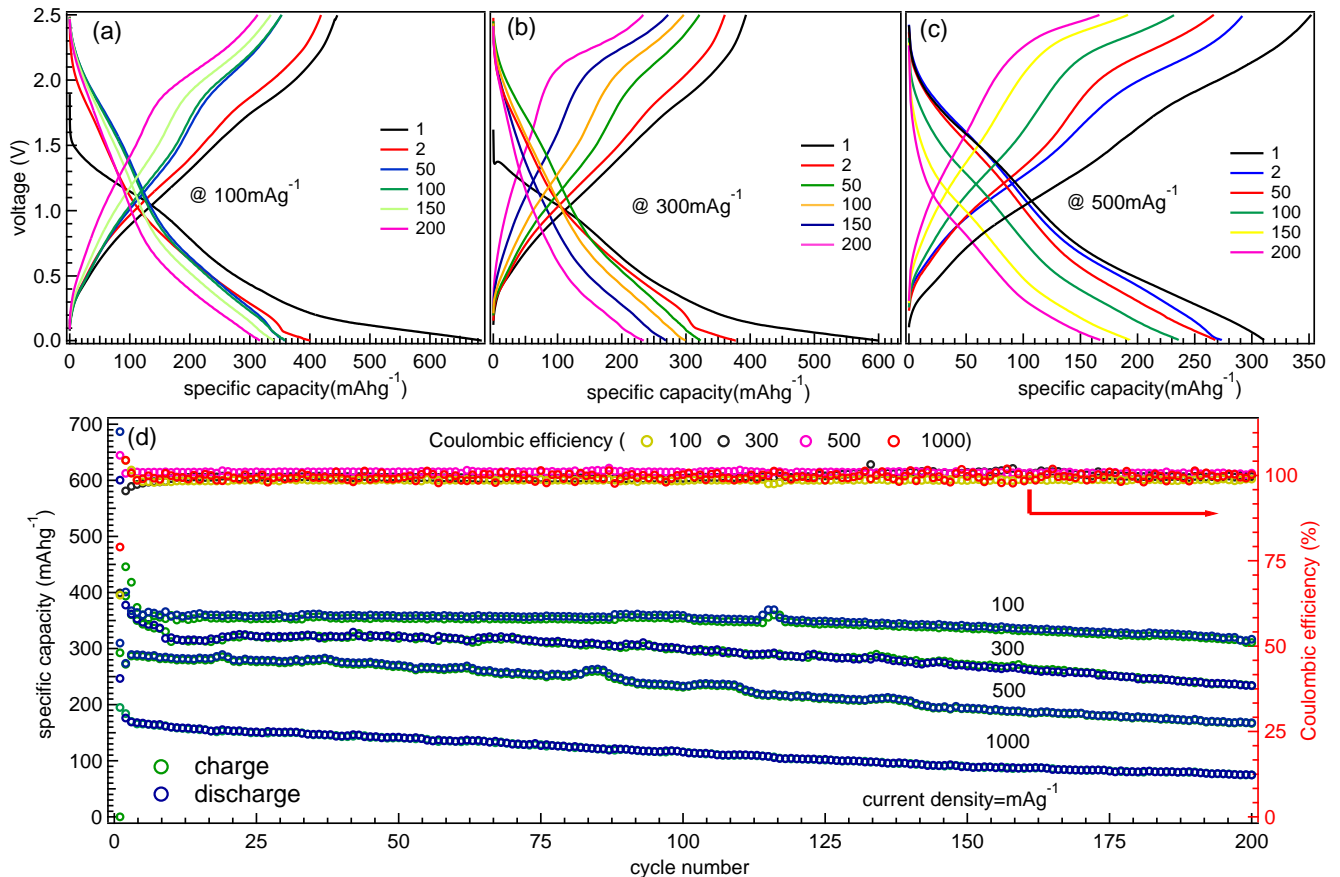


FIG. 3. The GCD curves of Al-MoS₂@rGO electrodes for selected cycles at a current density of (a) 100 mA g⁻¹, (b) 300 mA g⁻¹, and (c) 500 mA g⁻¹. (d) The specific capacity during long cycling up to 200 cycles at different current densities.

the formation of metallic Mo and Na₂S matrix, and the third plateau at 0.4-0.005 V represents the intercalation of Na-ion into the interface of Mo and Na₂S, as marked in Fig. 2(b). On the other hand, the sloping region at 1.9 V is clearly visible in case of charge, representing the reversible oxidation of Mo to MoS₂. We find a significant enhancement in the electrochemical performance of Al-MoS₂@rGO composite due to its stable metallic 1T phase with a larger interlayer spacing. The first discharge specific capacity is found to be 703 mAh g⁻¹ at the current density of 50 mA g⁻¹, which is higher than the theoretical specific capacity of MoS₂ (670 mAh g⁻¹, this theoretical capacity is evaluated on the basis of conversion reaction between one MoS₂ molecule and four sodium ions). The stable specific capacity retention of about 400 mAh g⁻¹

was observed at 50 mA g⁻¹ in the following cycles. The additional capacity obtained in the first discharge cycle may be attributed to the formation of SEI layer at the electrode-electrolyte interface, which is caused by electrolyte reduction and also exposure to vacancy defects of rGO [66].

The remarkable rate performance of 1T Al-MoS₂@rGO anode is presented in Figs. 2(c, d). Here, we observe high rate capability at different current densities of 50, 100, 300, 500, 800 and 1000 mA g⁻¹, approaching 446 mAh g⁻¹ at 50 mA g⁻¹ to a specific capacity of 169 mAh g⁻¹ at 1000 mA g⁻¹ and the corresponding GCD profiles are shown in Fig. 2(d) for the second cycle at each current density. The electrodes display 91% and 95% specific capacity retention as the

current density returns to 50 and 100 mA g^{-1} indicating high stability of the formed SEI layer in FEC added electrolyte [35]. In order to elucidate the long stability of the cell performance, Figs. 3(a, b, c) display the GCD profiles for every 50th cycle at current densities of 100, 300 and 500 mA g^{-1} , respectively. The GCD curves in Fig. 3(c) are measured on the same cell after 5 cycles at 50 mA g^{-1} (shown in Fig. 3(a) of [61]). Moreover, the long cycling performance of Al-MoS₂@rGO anode is shown in Figs. 3(d) at different current density over 200 cycles. The composite as an anode shows capacity retention of 86%, 66%, 58%, and 45% at the current densities of 100, 300, 500, and 1000 mA g^{-1} with almost 100% Coulombic efficiency, showing better stability at slower current rates. The Al doping in MoS₂@rGO lowers the activation barrier of Na-ion for ease insertion/extraction into the host-structure by increasing the interlayer distance, which improves the specific capacity and stability. However, the slow capacity fading during the long cycling process, as shown in Fig. 3 of [61], may involve some polarization effect, surface stability as well as the transition-metal cation (Mo) dissolution leading the formation of a thick SEI layer [67]. Here, the particle size, surface engineering by decorating conducting materials as well as morphology control may help to further improve the cyclic stability [68].

3.3 Analysis of cyclic voltammetry data:

Further, to explore the sodium-ion storage mechanism in Al-MoS₂@rGO anode, the kinetic behavior of the ions is studied by detailed CV measurements performed at various scan rates ranging from 0.08 to 0.7 mVs⁻¹ in a voltage window of 0.005–2.5 V, as presented in Fig. 4(a). The diffusion coefficient is calculated using Randles-Sevcik equation as given below [69]:

$$i_p = (2.69 \times 10^5) AD^{\frac{1}{2}} C n^{\frac{3}{2}} \nu^{\frac{1}{2}} \quad (4)$$

where, i_p is the peak current (mA), A is the active surface area of the electrode (cm²), D is the diffusion coefficient (cm²s⁻¹), C is the sodium ion concentration in the bulk

(mol cm⁻³), n is the electron transferred in the redox reaction and ν is the scan rate (mVs⁻¹). In order to calculate the value of D , we fit the oxidation/reduction peak current versus square root of ν with linear behavior, as shown in Fig. 4(b) and the slope is extracted. The D values were found to be 1.60×10^{-10} and 0.91×10^{-10} cm²s⁻¹ correspond to the anodic and cathodic peaks, respectively. In the anodic case, the relatively fast Na-ion kinetics is due to the disappearance of non-conductive Na₂S [39, 65], which is also consistent with the gradual decreasing trend of resistance in the EIS spectra during the charging from 0.005 to 2.5 V [as shown later in Figs. 5(b, d)].

Moreover, the current response of the electrode at different potentials can be attributed to the surface-controlled and diffusion-controlled currents. The net current obeys the following relation [70]:

$$i = a\nu^b \quad (5)$$

where i is the net current in mA, ν (mVs⁻¹) is the scan rate and a and b are adjustable parameters. Here, we can identify different charge storage mechanisms by the value of b , which normally varies between 0.5 to 1; for example, $b = 0.5$ represents a diffusion-controlled mechanism and $b = 1$ represents a surface capacitive current. It is important to note that the value of b can be obtained by the slope of liner fitting of $\log(\text{peak current } i_p)$ versus $\log(\nu)$, as shown in Fig. 4(c). The obtained values of b for anodic peaks (A) and cathodic peaks (C) are 0.98 and 0.82, respectively, suggesting the pseudo-capacitive behavior of the Al-MoS₂@rGO electrode, which shows a faradic like charge storage mechanism with capacitor like electrochemical response. This type of behavior is basically observed in nano-structured MoS₂, which enable the system to achieve high energy and power densities [71]. Moreover, based on the previously reported analysis by Dunn and his co-workers, the current response during voltage sweep can be written as the sum of both capaci-

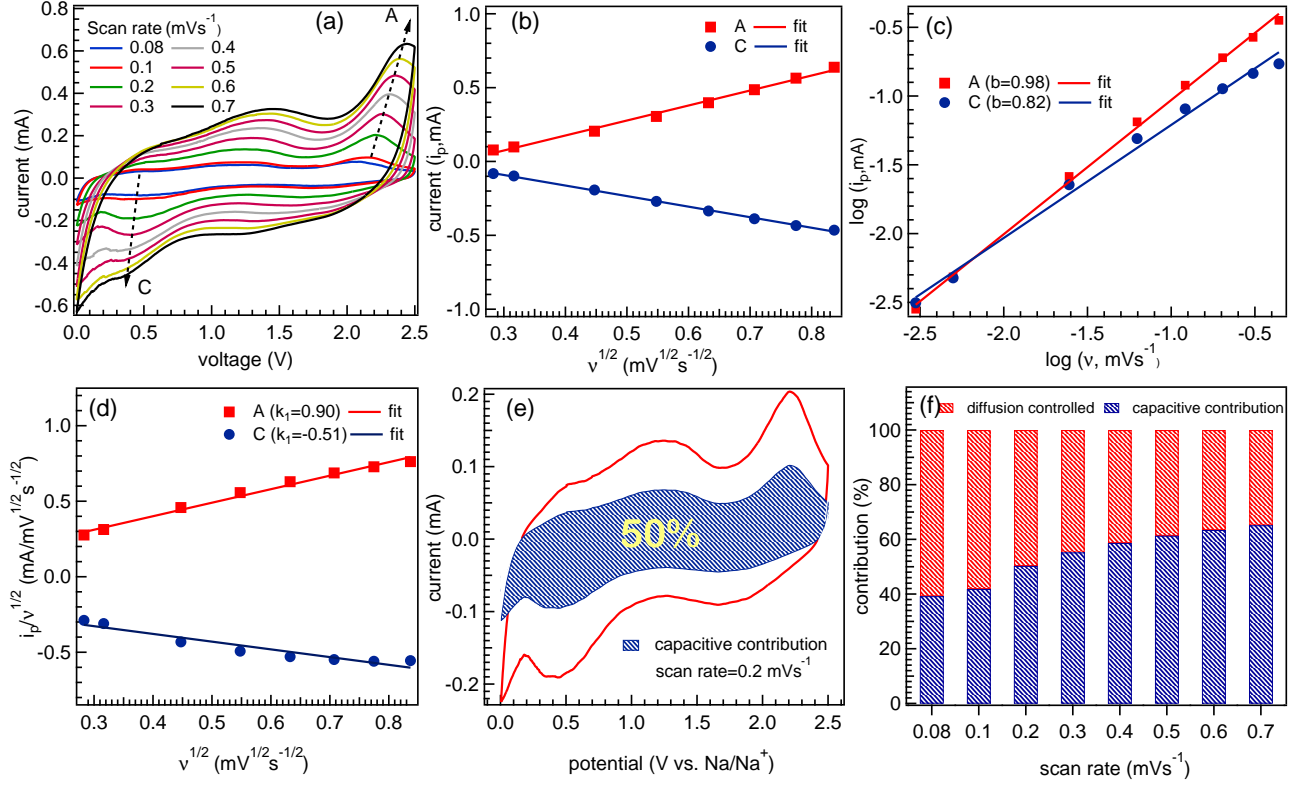


FIG. 4. (a) The cyclic voltammograms of Al-MoS₂@rGO at different scan rates ranging from 0.08 to 0.7 mVs⁻¹ in a potential window of 0.005–2.5 V, (b) the linear fit between peak current i_p and square root of scan rate, and (c) the linear fit between $\log(i_p)$ and $\log(\nu)$ for different scan rates, (d) the linear fit between $i_p/\nu^{1/2}$ and $\nu^{1/2}$ for different scan rates, (e) the shaded area showing capacitive contribution at a scan rate of 0.2 mVs⁻¹, and (f) the capacitive and diffusive contributions for the total current extracted at various scan rates.

tive and diffusive current, as given below [26, 72, 73]:

$$i = k_1\nu + k_2\nu^{1/2} \quad (6)$$

After rearranging the above equation, we can write as:

$$i/\nu^{1/2} = k_1\nu^{1/2} + k_2 \quad (7)$$

where, k_1 and k_2 are the adjustable parameters and $k_1\nu$ and $k_2\nu^{1/2}$ show the contribution from capacitive and diffusive currents, respectively. To calculate the value of k_1 and k_2 , we perform the linear fit to the peak current $i_p/\nu^{1/2}$ versus $\nu^{1/2}$ plot, as shown in Fig. 4(d). The slope and intercept of the line give the values of k_1 and k_2 , respectively. The obtained values of k_1 for anodic/cathodic peaks are found to be 0.90/0.51, respectively. Using the values of k_1 and k_2 , the calculated

capacitive and diffusive contributions are found to be 50% each, as plotted for the scan rate of 0.2 mVs⁻¹ in Fig. 4(e). The variation in the diffusive and capacitive contributions (in percentage scale) for different scan rates is shown in Fig. 4(f), where 0.7 mVs⁻¹ attributes lowest diffusion controlled current. The increasing trend of capacitive contribution indicates that at higher scan rates most of the charge is being stored by the surface redox reaction.

3.4 Electrochemical impedance spectroscopy:

To reveal the electrochemical reaction kinetics of the 1T phase Al-MoS₂@rGO composite, the EIS measurements are performed at room temperature in the fre-

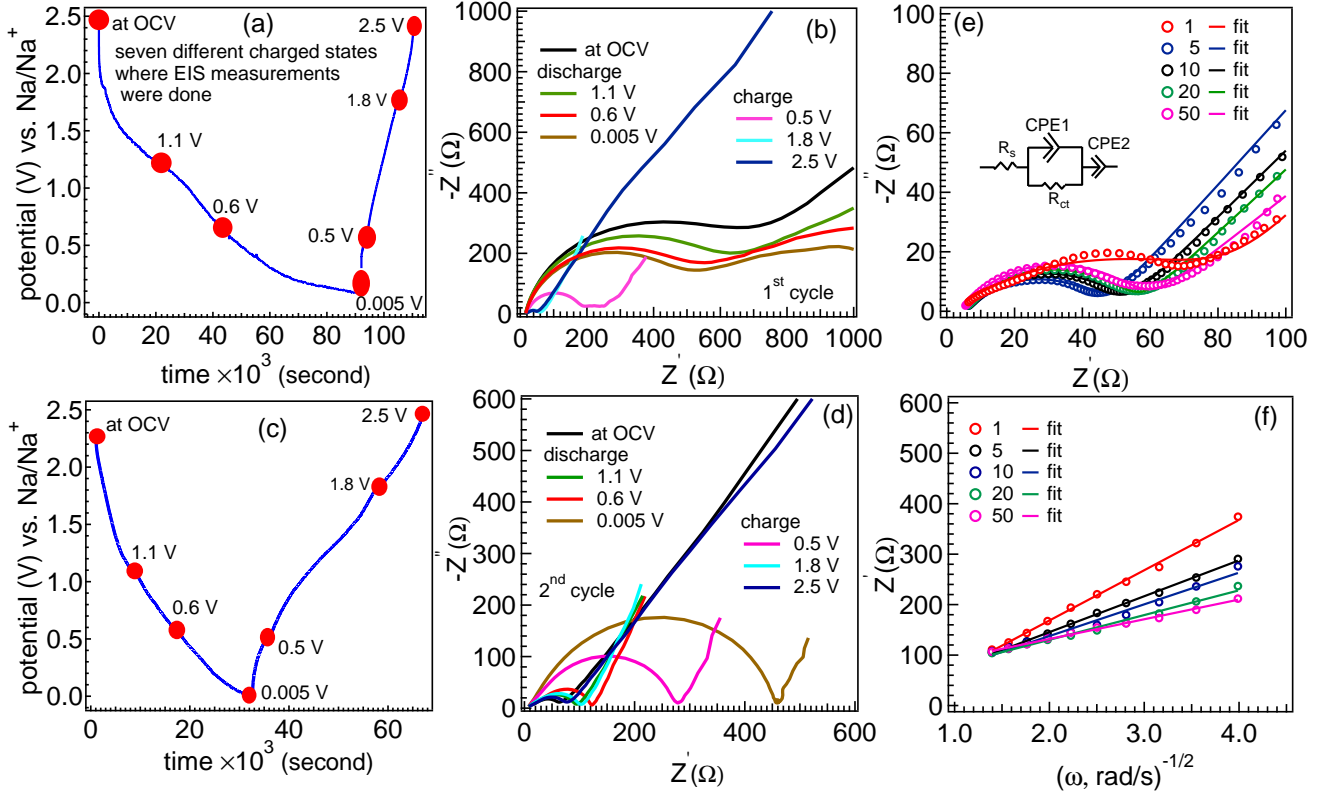


FIG. 5. The gavanostatic charge-discharge profile of the (a) first cycle and (c) second cycle with seven different points marked where the EIS measurements are carried out. The *in-situ* Nyquist plot during the (b) first cycle and (d) second cycle at different critical voltages ranging from OCV to fully sodiated/discharged state (0.005 V), and then fully desodiated/charged state (2.5 V), (e) the fitted Nyquist plots, with the corresponding equivalent circuit, measured in fully discharged states after 1st, 5th, 10th, 20th and 50th cycles of GCD at 500 mA g⁻¹, (f) the plot of the real part of impedance versus the inverse square root of angular frequency in Warburg region at different cycles obtained from data in (e).

quency range of 100 kHz to 10 mHz at seven different states during the first sodiation/de-sodiation cycle, as marked across the potential vs time curve in Fig. 5(a). The corresponding Nyquist plot at OCV in Fig. 5(b) consists of a compressed semicircle in the high and middle range of frequency regions, which are attributed to the charge transfer resistance (R_{ct}) and R_{SEI} at the electrode-electrolyte interface and the straight line in the low-frequency region is related with the diffusion of sodium-ion in the bulk region of electrode material. During the first discharge from 1.1 V to 0.005 V (as shown in Fig. 5(b)), nearly two semicircles are evolved in the high and mid frequency range, depicting the SEI formation and the intercalation of sodium-ion in the MoS₂ host

matrix. Also, the non-conductive Na₂S matrix due to the constant volume change of the active material occurring during discharging of the cell. The formation of nano-clusters like Na_xMoS₂ gradually decreases the charge transfer resistance during de-sodiation. However, in the case of charging, the semi-circle in the intermediate frequency range disappears and a single semi-circle formed in the entire frequency region, elucidating the dominance of charge transfer resistance over the SEI impedance [74]. The subsequent decrement in the diameter of the semicircle, when charging from 0.5 V to 2.5 V, shows the dissolution of the thick SEI layer. Note that the first cycle is also complicated having some irreversible nature possibly due to SEI formation and electrolyte reduction, which is also

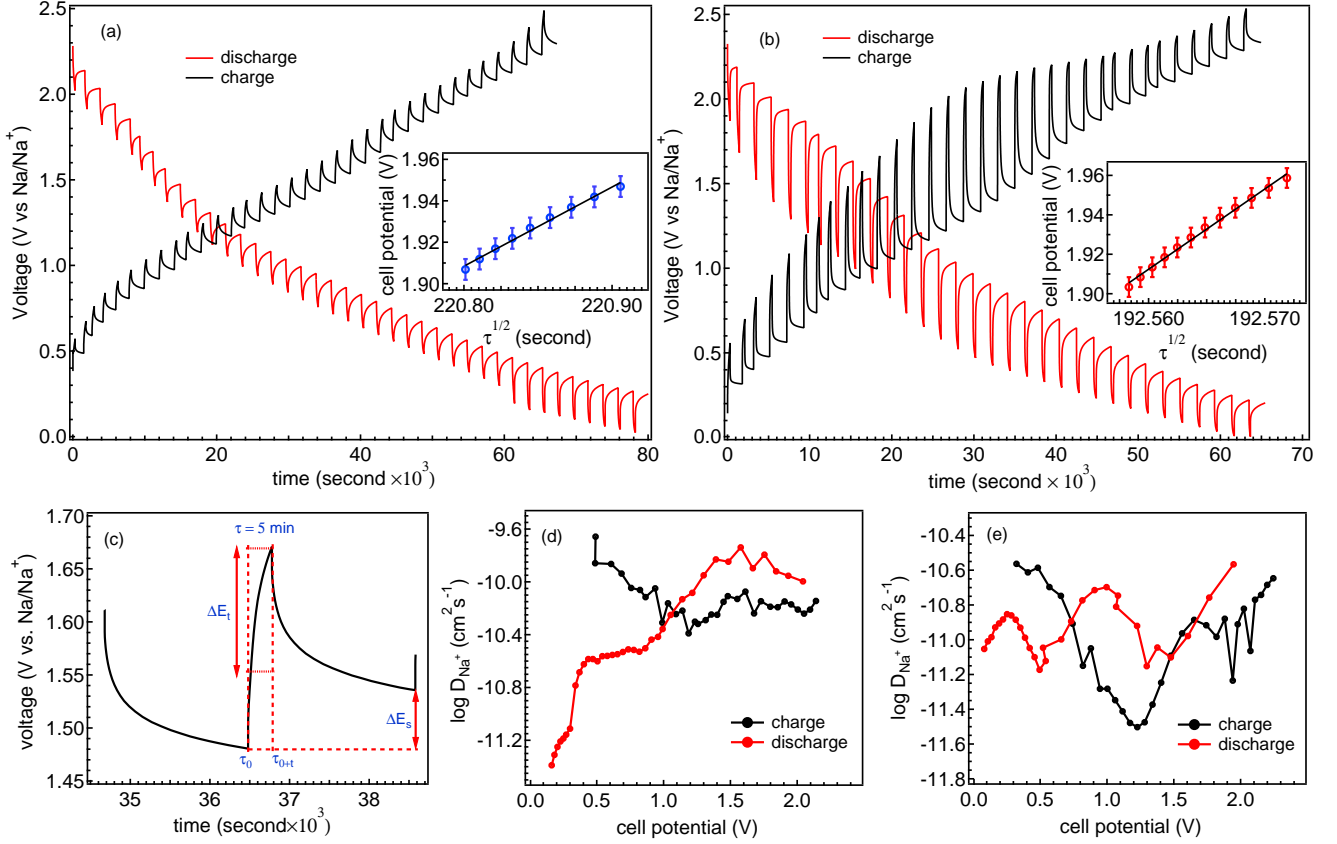


FIG. 6. The GITT measurements of Al-MoS₂@rGO electrodes at a current density of 500 mA g⁻¹ in a voltage window of 0.005–2.5 V (a) during 4th cycle, and (b) 500th cycle, (c) a schematic labeling of different parameters of a single titration curve before, during and after application of a current pulse for 5 min. The logarithmic diffusion-coefficient profile as a function of cell voltage during charge–discharge for 4th cycle in (c), and for 500th cycle in (d).

reflected in Fig. 5(b) where the R_{ct} found to decrease with discharge/charge voltages. Therefore, to understand the reaction mechanism in more stable state, we present the similar data on a fresh cell for the 2nd cycle in Figs. 5(c, d), which clearly show the increasing/decreasing trend in the R_{ct} values during discharge/charge process confirming the reversible mechanism from second cycle.

Furthermore, the EIS measurements are performed to study the variation in R_{ct} values and diffusion coefficient after several cycles where the Nyquist plots are shown in Fig. 5(e). The value of the physical components corresponding to different regions can be calculated by fitting the equivalent circuit model [43], as shown in the inset of Fig. 5(e) at different cycles. Here, the high value of R_{ct} in 1st cycle as compared to the 5th cycle is a bit unusual

and not consistent with the observed specific discharge capacity during the initial cycles, as shown in Fig. 3(a) of [61]. This could be due to several reasons like complex reaction at electrode/electrolyte interface; however, a similar observation in refs. [75, 76] is said to be the activation process during initial cycle(s). After the 5th cycle, the subsequent increase in the R_{ct} value determines the in-filtration of sodium-ion and the formation of high activation barrier to hinder the sodium-ion kinetics. This phenomenon proves that the surface stability of MoS₂ decreases during cycling, which is consistent with the long cycling measurement of MoS₂, as shown in Fig. 3(d). The diffusion coefficient of sodium-ion in the bulk of Al-MoS₂@rGO electrode can be calculated by the following

equations [77]:

$$D_{\text{Na}^+} = R^2 T^2 / 2n^4 F^4 \sigma_w^2 A^2 C^2 \quad (8a)$$

$$Z' = R_s + R_{ct} + \sigma \omega^{-0.5} \quad (8b)$$

where R , T , n , F , σ_w , A , and C , are the universal gas constant ($8.314 \text{ J mol}^{-1} \text{ K}^{-1}$), temperature, the number of electrons exchanged in the reaction, the Faraday's constant (96485 C mol^{-1}), the Warburg coefficient ($\Omega - s^{-1/2}$), the surface area of the electrode (1.13 cm^2) and the Na-ion concentration in the electrode material ($\text{mol}\cdot\text{cm}^{-3}$), respectively. The Warburg coefficient σ_w is related to the real part of impedance (Z') by equation 8, where R_s is the solution resistance. In order to calculate the D_{Na^+} , the real part of impedance is plotted as a function of the inverse square root of angular frequency $\omega^{-1/2}$ in the Warburg region at different cycles and fitted linearly as shown in Fig. 5(f). The values of the apparent sodium diffusion coefficient are found to be in the range from 0.18×10^{-11} to $1.84 \times 10^{-11} \text{ cm}^2 \text{ s}^{-1}$.

3.5 Galvanostatic intermittent titration technique (GITT) investigation:

The chronopotentiometry based GITT measurements were performed on the electrode to demonstrate the structural evolutions and the origin of the electrochemical kinetics during the Na-ion insertion/extraction process. Figs. 6(a, b) elucidate the overall potential response profiles as a function of time at 4^{th} cycle and 500^{th} cycle, respectively, and are consistent with the galvanostatic charge-discharge curves. The GITT measurements were carried out by first charging the cells with a current density of 500 mA g^{-1} to maximum cut-off voltage for a short duration of 5 min, which was followed by a relaxation period of 30 min to reach a steady-state value (E_s), then the same condition was repeated to discharge the cells up to the minimum voltage. To calculate the diffusion coefficient under thermodynamic equilibrium conditions, the Fick's second law of diffusion is simplified by using

the following equation with some assumptions [78].

$$D_{\text{Na}^+} = \frac{4}{\pi \tau} \left[\frac{m V_M}{M A} \right]^2 \left[\frac{\Delta E_s}{\tau (\Delta E_t / d \sqrt{\tau})} \right]^2 \quad (9)$$

where, $\tau = L^2 / D_{\text{Na}^+}$, L is the diffusion length of sodium ion (thickness of the electrode), V_M ($\text{cm}^3 \text{ mol}^{-1}$) is the molar volume of Al-MoS₂@rGO composite, which is deduced using the equation " $N_A * V_{unit} / Z$ " (here N_A is the Avogadro's number, V_{unit} is the volume of a unit cell and Z is the number of unit cells). The m (gm) and M (gm mol⁻¹) are the mass and molecular weight of Al doped MoS₂, respectively, A is the active surface area between the electrode and electrolyte, ΔE_s and ΔE_t are the changes in steady-state voltage after the OCV stand of 30 min, and the transient change in voltage due to the current pulse after excluding the IR drop, respectively, as depicted in Fig. 6(c). Here, the molar volume is assumed to be constant with the variation of the state of charge (SOC) for diffusion coefficient calculation. The insets of Figs. 6(a, b) shows a linear relationship between the variation of cell voltage and the square root of time ($\tau_{1/2}$), which is used as a fact to simplify the equation 9, and that can be written as below:

$$D_{\text{Na}^+} = \frac{4}{\pi \tau} \left[\frac{m_B V_M}{M_B A} \right]^2 \left[\frac{\Delta E_s}{\Delta E_t} \right]^2 ; \tau = L^2 / D_{\text{Na}^+} \quad (10)$$

The Na-ion diffusion coefficient profiles as a function of cell voltage during charge and discharge processes for 4^{th} and 500^{th} cycles are shown in Figs. 6(d, e), respectively. In the case of discharge process, the diffusion coefficient of Na⁺ gradually decreases, showing a gradual increment of over-potential during insertion of sodium ions into Al-MoS₂@rGO host. However, the charging process shows a stable profile, elucidating lower potential barriers for sodium-ions. The diffusion coefficient profile for 500^{th} cycle, as demonstrated in Fig. 6(e) represents slightly slow diffusion of Na-ions in the host structure, i.e., diffusion coefficient is somewhat lower than the 4^{th} cycle. These results are consistent with the long cycling data in Fig. 3, where there is a gradual degradation in capacity after 200 cycles. The minimum in the profile depicts

the phase transition points, leading to strong interactions between sodium-ion and the host matrix.

3.6 Post cycling XRD and FESEM:

The post-cycling tests are carried out to investigate the effect of cycling on the structure and morphology of the extracted active material. We have dismantled the cell after 500 cycles at a current density of 500 mA g^{-1} and washed the electrode with DEC to retrieve the active material. Fig. 7(a) depicts the XRD pattern, which shows

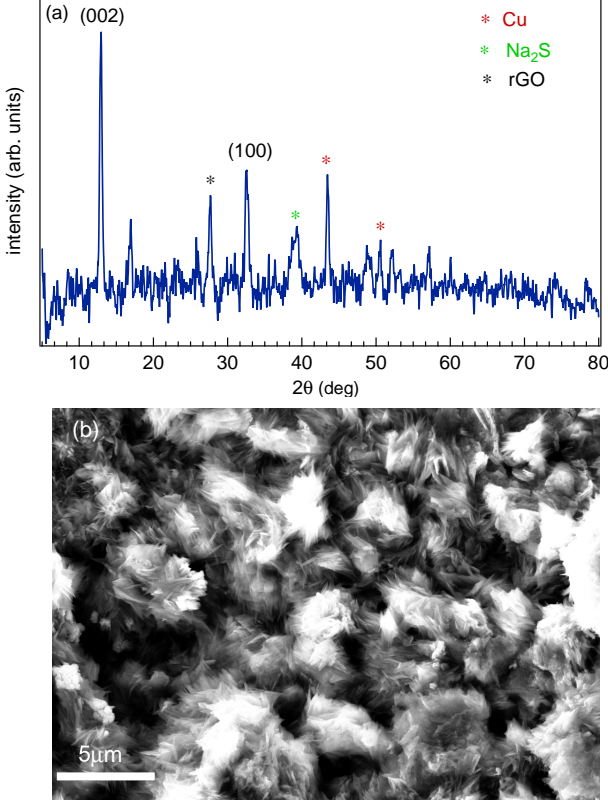


FIG. 7. (a) The XRD pattern and (b) the corresponding FE-SEM image of extracted active material from the cell after 500 cycles at a current density of 500 mA g^{-1} .

the peaks located at 14° and 33.3° that are attributes to the (002) and (100) planes, indicating the crystalline nature of the MoS_2 after cycling. The (220) peak at 39° (JCPDS No.03-0933) reflects the existence of Na_2S due to the incomplete reaction after cycling [39] and some peaks at around 43° and 51° are observed from the Cu-

foil [35]. The shifting of (002) peak towards higher 2θ suggests for a structural transformation of some percentage of 1T phase to 2H phase in the active material, which can be the primary cause of capacity fading after long cycling. The corresponding FE-SEM image is shown in Fig. 7(b) where the morphology of the active material indicates no cracking and discontinuity in the structure, which attributes to the corresponding capacity retention of the composite at 500 mA g^{-1} after long cycling.

3.7 X-ray photoemission spectroscopy study:

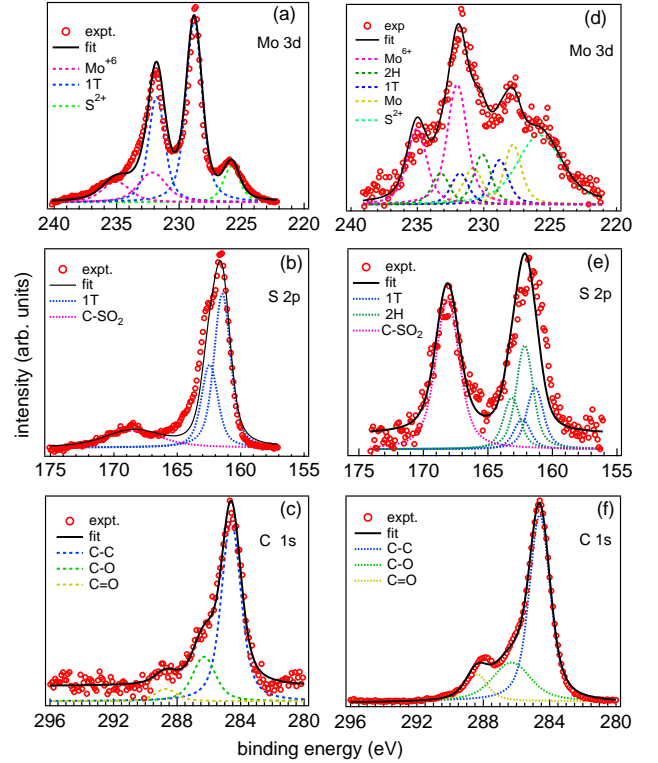


FIG. 8. The Mo $3d$, S $2p$ and C $1s$ core-level XPS spectra of Al- MoS_2 @rGO pristine sample (a-c) as well as powder extracted from electrode after long cycling (d-f), respectively.

We use x-ray photoelectron spectroscopy (XPS) to investigate the electronic structure of Al- MoS_2 @rGO pristine sample as well as after long cycling. In Fig. 8(a), the Mo $3d$ core-level of pristine sample consists of two spin-orbit coupled peaks $3d_{5/2}$ and $3d_{3/2}$ at the binding energies around 228.8 eV and 231.8 eV, respectively, which are consistent and confirm the presence of Mo in 4+ ox-

idation state [33, 77, 79]. The de-convoluted peaks that detected around 232.1 eV and 235 eV could be related to MoO_3 or MoO_4^{2-} , which are found during the decomposition of Mo precursor $(\text{NH}_4)_6\text{Mo}_7\text{O}_{24}\cdot 4\text{H}_2\text{O}$ in the hydrothermal synthesis [80]. Also, we can clearly observe S $2s$ core-level at binding energy (BE) of 225.8 eV, which originate from the sulfide species [81]. In case of the S $2p$ spectrum of pristine sample, as shown in Fig. 8(b), there are two intense peaks at BEs around 161.4 and 162.4 eV denoting the S $2p_{3/2}$ and S $2p_{1/2}$ doublet, respectively, of the S^{2-} oxidation state. The peak located at 168.5 eV can be assigned to the sulfate groups [82]. The C $1s$ core-level of pristine sample is displayed in Fig. 8(c) where the most intense peak at 284.6 eV indicates the C-C bonding, and the peaks located at 286 eV and 288.7 eV can be ascribed to the oxygenated functional groups C-O and C=O, respectively, which show the intercalative mixing of rGO and MoS_2 [80].

More importantly, we perform the XPS measurements (*ex-situ*) of anode powder that was extracted from the electrode after long cycling, which reveal the presence of both 1T and 2H phases of MoS_2 due to the transition reaction mechanism in 1T- MoS_2 after long cycling. Note that the Mo $3d$ orbitals of trigonal prismatic co-ordinated 2H- MoS_2 splits in to three degenerate energy levels forming (i) d_{z^2} , (ii) $d_{xy} + d_{x^2-y^2}$ and (iii) $d_{yz} + d_{xz}$ due to crystal field splitting and there is a finite energy gap of ~ 1 eV between the first two orbital sets. Moreover, the two Mo d electrons fill the lower d_{z^2} orbital, indicating the semi-conducting behavior of 2H- MoS_2 . However, in case of 1T- MoS_2 , there are two degenerate energy levels namely, (i) $d_{xy} + d_{yz} + d_{xz}$ and $d_{z^2} + d_{x^2-y^2}$ due to the octahedral co-ordination and having two un-paired electrons in the lower ($d_{xy} + d_{yz} + d_{xz}$) orbitals make the 1T- MoS_2 metallic [83, 84]. The more conductive nature of 1T- MoS_2 helps to enhance the electro-chemical kinetics due to fast electron transfer process as compared to the 2H- MoS_2 . The intercalation of sodium-ions during cycling form the stable 2H phase

and metastable 1T phase due to the charge transfer from alkali metal atoms to the MoS_2 nano-sheets. Fig. 8(d) depicts the Mo $3d$ spectrum of cycled material, where the co-existence of both 1T (octahedral) and 2H (trigonal) phases in the nano-sheets forming a 2D in-plane 1T/2H hetero-structure is clearly visible. The evolution of a peak at 227.8 eV gives a clear evidence of the presence of Mo $3d_{5/2}$, which is formed during the conversion reaction of Na_xMoS_2 [85]. According to the composition, the cycled material consists of Na_2MoO_4 , 1T- MoS_2 and 2H- MoS_2 . Moreover, the Mo^{6+} always exist in both pristine and cycled material indicating the formation of MoO_4^{2-} where the Na_2MoO_4 acts as a protective sheath and provides stability during long cycling [85]. Further, the S $2p$ core-level of cycled anode material is shown in Fig. 8(e), which indicates the evolution of a pair of new peaks (at 162.2 eV and 163.2 eV for the doublet $2p_{3/2}$ and S $2p_{1/2}$, respectively). These components are consistent with the presence of 2H phase after long cycling and observed a shift of 0.8 eV towards higher BE as compared to the peaks of 1T- MoS_2 (at 161.4 and 162.4 eV) phase [86]. Moreover, the Al $2p$ core-level of cycled material is found to be at 74.5 eV BE, see Fig. 4 of [61], which indicates the bonding between Al and S in the anode material. Fig. 8(f) shows the C $1s$ core-level spectrum of the cycled anode material where there is no shift in the peak positions as compared to the pristine material, indicating no change in oxidation state and stable nature of rGO. The evolution of mixed 1T/2H phase after long cycling affects the electrochemical performance owing to the formation of less conductive 2H- MoS_2 phase [87], which is compatible with the long cycling results in Fig. 3.

3.8 Theoretical results and discussion:

Finally, using density functional theory (DFT) we investigate the Na-ion migration in 1T phase of Al- MoS_2 @rGO interface and Al- MoS_2 - MoS_2 interlayer host structures. We consider a monolayer MoS_2 supercell by cleaving a layer from the primitive unit cell of MoS_2 . The unit cell of 1T- MoS_2 has one formula unit with hexa-

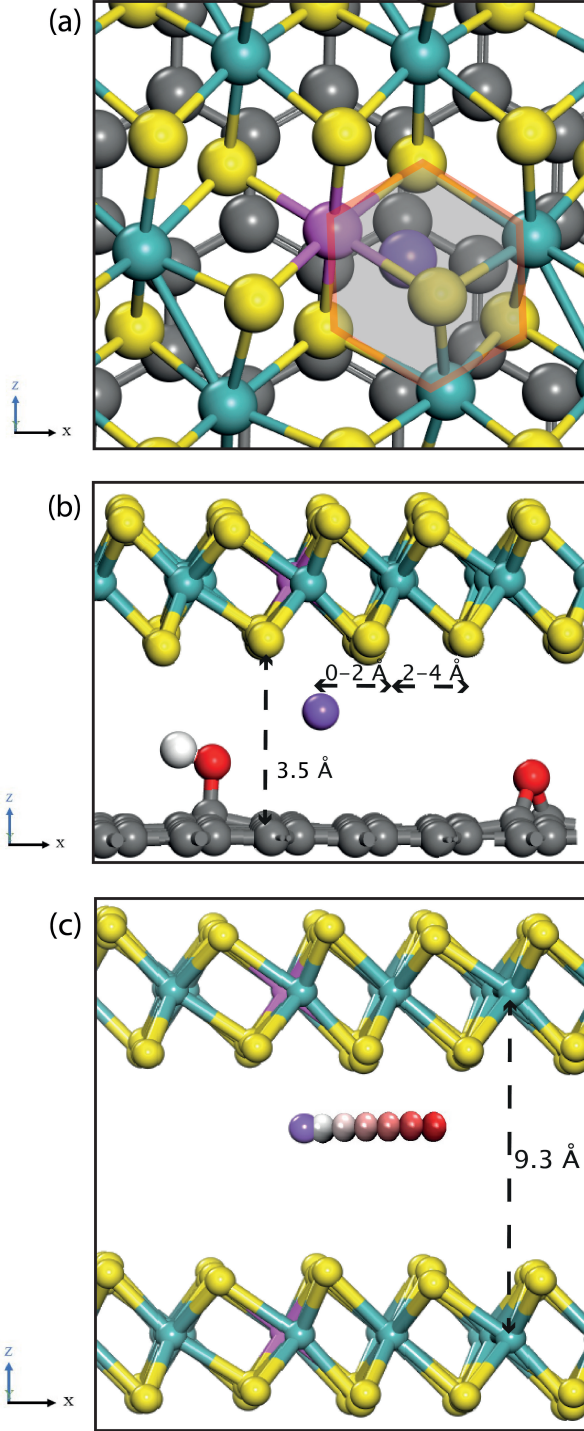


FIG. 9. (a) The top view of sodium atom (blue) at 2H site in the host Al (purple) doped 1T-MoS₂@rGO structure where grey hexagonal block shows the coordination of sodium with MoS₂ having Mo (cyan), S (yellow), C (black), O (red) and H (white). (b) The front view of optimized structure of sodium-ion intercalation in layered 1T phase of Al-MoS₂@rGO interface, where the sodium-ion activation barrier is visible. (c) The sodium-ion migration (blue-white-red) pathways in 1T Al-MoS₂@rGO interlayer and the activation barrier of sodium-ion along the migration path.

coordinate geometry corresponding to the $P\bar{3}m1$ space group [88]. Here the bonding of Al and S is considered based on the XPS measurements, which are consistent with the observation in ref. [89] that the Al bonded with S atoms when doped in MoS₂. Also, the DFT calculations have further confirmed a greater stability of Al doping at the Mo site, which is bonded with the S atoms [90, 91], as shown in Fig. 9(a). The rGO is modelled in a supercell with approximately similar lattice parameters to that of MoS₂ supercell. The optimised structures are considered for the formation of layered 1T-MoS₂ at rGO layer with the initial interspace distance (distance between a carbon atom of rGO and its nearest S atom of MoS₂ layer) of 3.5 Å. Here, the layering of Al-MoS₂ bulk and rGO is formed as an extended layer, one above the other with slight difference in the lattice parameters of individual structures but, the binding energy of this system is comparable with that of MoS₂/graphene interface, after the geometry optimisation of the structure [46]. This initial interspace distance is used for the optimization of 1T-MoS₂@rGO as the stable configuration, which is similar to the one obtained in MoS₂/graphene structure [92]. In order to introduce the sodium-atom in the structure, four different sites are available as explored by Massaro and co-workers on sodium-ion intercalation in the host MoS₂/graphene interface, which were explained as hollow-edge, hollow-hollow, top-edge and top-hollow where the sodium could be introduced between MoS₂-graphene layer. Interestingly, the calculated sodium-ion intercalation energy (ΔE_{int}) is to be the same and all these sites are considered stable sites for sodium atoms [46]. In the present work, the sodium-ion is introduced on structural optimization of Al-MoS₂/rGO composite at the hollow-hollow site, which comprised of one of the four sites mentioned above, see Fig. 9(a). The intercalation energy of sodium-ion at these sites is calculated by using the equation [$\Delta E_{\text{int}} = E_{\text{Na@site}} - E_{\text{site}} - E_{\text{Na}}$]. The sodium sites have intercalation energy of -87.61 kJ/mol (= -0.908 eV), which is comparable to that

of MoS₂/graphene and considered a stable site for sodium atom in the host Al-MoS₂@rGO structure. The optimized structure of 1T Al-MoS₂@rGO interface is shown in Fig. 9(b).

Moreover, the sodium-ion migration is performed along the x -axis for migration distances corresponding to 0–2 Å and 2–4 Å where the reference is considered as the initial ($x = 0$) position of sodium-ions at the hollow-hollow site, as represented in Fig. 9(a). An estimate for sodium-ion diffusivity is obtained using an Arrhenius type fit [93] $D_{Na^+} = D_0 \exp(-E_{act}/k_B T)$, where $D_0 = a^2 v$, a = sodium-ion migration length, v = phonon frequency ($\sim 10^{13}$ Hz) [52], E_{act} = activation energy, k_B is the Boltzmann constant and T is the temperature. At 300 K ($k_B T = 0.0265$ eV), the activation energies of sodium-ion are calculated as ~ 57.9 kJ/mol and ~ 40.3 kJ/mol in 1T Al-MoS₂@rGO interface for $a = 0-2$ Å and $a = 2-4$ Å, respectively. For the comparison, we have shown the activation energy values of un-doped 1T phase of MoS₂/rGO composite, which are found to be ~ 68.3 kJ/mol and ~ 50.2 kJ/mol for $a = 0-2$ Å and $a = 2-4$ Å, respectively. This suggests that the Al doped 1T phase have lower energy barrier as compared to the un-doped system. From the calculated activation energies using DFT, the corresponding diffusion coefficient of sodium-ions (D_{Na^+}) are estimated as $\sim 10^{-13}$ and $\sim 10^{-10}$ cm²/s, respectively, which are comparable with the experimental values and indicate the faster diffusion of sodium-ion in the doped system. Note that the DFT simulations suggest that the sodium-ion activation energies vary from ~ 40.3 kJ/mol to ~ 57.9 kJ/mol with respect to the sodium-ion migration in 1T phase Al-MoS₂@rGO interface system and corresponding fits for D_{Na^+} may vary from $\sim 10^{-10}$ cm²/s to $\sim 10^{-13}$ cm²/s. For the second model, the 1T phase Al-MoS₂-MoS₂ interlayer, a similar procedure is followed to study the sodium-ion migration. The inter-layer distance (between two Mo atoms along c -axis) of 9.3 Å is considered for DFT calculations, similar to the

distances indicated in the experiment. The activation energies for sodium-ion migration are estimated as ~ 49.8 kJ/mol to ~ 59.6 kJ/mol, respectively for the aforementioned initial migration distances, i.e., from $a = 0-2$ Å to $a = 2-4$ Å. Fig. 9(c) shows the pathways of sodium-ion along the x -direction in the structure. The corresponding D_{Na^+} values are estimated in the range of $\sim 10^{-11}$ – 10^{-13} cm²/s, which suggests that sodium-ion transport is enhanced when moving from bulk to 2D layered structure [94].

IV. CONCLUSION

The 1T phase of 5% Al doped MoS₂@rGO was synthesized successfully through the hydrothermal route, which resulted in the larger interlayer distance of around 0.93 nm and the morphological studies confer the 3-D nano-flower-like architecture of the composite. This composite material as an anode for SIBs has displayed the first discharge specific capacity of about 764 mAhg⁻¹ with a reversible capacity retention of 383 mAhg⁻¹ over 10 cycles at a current density of 50 mA g⁻¹. We observed capacity retention of 86%, 68%, 58%, and 45% at current densities of 100, 300, 500, and 1000 mA g⁻¹ respectively, when the composite electrode was cycled over 200 cycles for stability test. The CV, EIS, and GITT analyses are performed to explore the sodium ion storage and diffusion mechanism in the composite host material. The calculated diffusion coefficient was found to be in the range of 10^{-10} – 10^{-12} cm²s⁻¹ depending on the respective parameter of the experiment. The enhanced electrochemical performance of 1T phase Al-MoS₂@rGO composite is attributed to the collaborative effect of enlarged interlayer distance and larger electronic conductivity, which facilitate the storage of sodium ions and electron transportation. These results further motivate to explore 1T phase of 2D layered material as anode for sodium-ion batteries. The *ex-situ* XPS study confirm the presence of both 1T

and 2H phases in the anode material, which reflects the small capacity fading after long cycling. The sodium-ion activation energies for migration in the layered 1T phase Al–MoS₂@rGO interface and Al–MoS₂–MoS₂ interlayer host structure are estimated using DFT.

V. ACKNOWLEDGMENTS

This work and setting-up the research facilities for sodium-ion battery project at IIT Delhi are financially supported from DST through “DST–IIT Delhi Energy Storage Platform on Batter-

ies” (project no. DST/TMD/MECSP/2K17/07) and from SERB-DST through core research grant (file no.: CRG/2020/003436). Manish, Jayashree and Jagdees thank MHRD, UGC, and DST (DST/TMD/MECSP/2K17/07), respectively for the fellowship. RSD and JKC thank IIT Delhi (IRD no. MI02186G) and NCTU, Taiwan, for the financial support through M-FIRP project. We thank IIT Delhi for providing research facilities for sample characterization (XRD and Raman scattering at the physics department, and FE-SEM and HR-TEM at CRF). The authors would like to acknowledge high performance computing (HPC) facility for all the computational work at IIT Delhi.

-
- [1] A. G. Olabi and M. A. Abdelkareem, Renewable energy and climate change, *Renew. and Sustain. Energy Rev.* 158 (2022) 112111.
- [2] D. Bogdanov, J. Farfan, K. Sadowskaia, A. Aghahosseini, M. Child, A. Gulagi, A. S. Oyewo, L. de S. N. S. Barbosa, and C. Breyer, Radical transformation pathway towards sustainable electricity via evolutionary steps, *Nat. Commun.* 10 (2019) 1077.
- [3] D. Tong, D. J. Farnham, L. Duan, Q. Zhang, N. S. Lewis, K. Caldeira, and S. J. Davis, Geophysical constraints on the reliability of solar and wind power worldwide, *Nat. Commun.* 12 (2021) 6146.
- [4] T. Mouais, O. A. Kittaneh, and M. A. Majid, Choosing the best lifetime model for commercial lithium-ion batteries, *Journal of Energy Storage.* 41 (2021) 102827.
- [5] Y. Yang, E. G. Okonkwo, G. Huang, S. Xu, W. Sun, and Y. He, On the sustainability of lithium ion battery industry – a review and perspective, *Energy Storage Materials.* 36 (2021) 186.
- [6] J.-M. Tarascon and M. Armand, Issues and challenges facing rechargeable lithium batteries, *Nature.* 414 (2001) 359.
- [7] B. Dunn, H. Kamath, and J.-M. Tarascon, Electrical energy storage for the grid: a battery of choices, *Science.* 334 (2011) 928.
- [8] M. Li, J. Lu, Z. Chen, and K. Amine, 30 years of lithium-ion batteries, *Advanced Materials.* 30 (2018) 1800561.
- [9] A. Hu, W. Chen, X. Du, Y. Hu, T. Lei, H. Wang, L. Xue, Y. Li, H. Sun, Y. Yan, J. Long, C. Shu, J. Zhu, B. Li, X. Wang, and J. Xiong, An artificial hybrid interphase for an ultrahigh-rate and practical lithium metal anode, *Energy Environ. Sci.* 14 (2021) 4115.
- [10] A. Hu, M. Zhou, T. Lei, Y. Hu, X. Du, C. Gong, C. Shu, J. Long, J. Zhu, W. Chen, X. Wang, and J. Xiong, Optimizing redox reactions in aprotic lithium–sulfur batteries, *Adv. Energy Mater.* 10 (2020) 2002180.
- [11] J.-M. Tarascon, Is lithium the new gold?, *Nature Chem.* 2 (2010) 510.
- [12] C. Grosjean, P. H. Miranda, M. Perrin, and P. Poggi, Assessment of world lithium resources and consequences of their geographic distribution on the expected development of the electric vehicle industry, *Renew. and Sustain. Energy Rev.* 16 (2012) 1735.
- [13] K. M. Abraham, How comparable are sodium-ion batteries to lithium-ion counterparts?, *ACS Energy Lett.* 5 (2020) 3544.
- [14] J. -Y. Hwang, S. -T. Myung and Y. -K. Sun, Sodium-ion batteries: present and future, *Chem. Soc. Rev.* 46 (2017) 3529.
- [15] E. Goikolea, V. Palomares, S. Wang, I. R. Larramendi, X. Guo, G. Wang, and T. Rojo, Na-ion batteries–

- approaching old and new challenges, *Adv. Energy Mater.* 10 (2020) 2002055.
- [16] M. Sawicki and L. L. Shaw, Advances and challenges of sodium ion batteries as post lithium ion batteries, *RSC Adv.* 5 (2015) 53129.
- [17] S. K. Sapra, J. Pati, P. K. Dwivedi, S. Basu, J.-K. Chang, R. S. Dhaka, A comprehensive review on recent advances of polyanionic cathode materials in Na-Ion batteries for cost effective energy storage applications. *Wiley Interdiscip. Rev. Energy Environ.* 10 (2021) e400.
- [18] J. Pati, Hari Raj, S. K. Sapra, A. Dhaka, A. K. Bera, S. M. Yusuf, and R. S. Dhaka, Unraveling diffusion kinetics of honeycomb structured $\text{Na}_2\text{Ni}_2\text{TeO}_6$ as a high-potential and stable electrode for sodium-ion batteries, *J. Mater. Chem. A* 10 (2022) 15460–15473.
- [19] K. Nobuhara, H. Nakayama, M. Nose, S. Nakanishi, and H. Iba, First-principles study of alkali metal-graphite intercalation compounds, *J. Power Sources.* 243 (2013) 585.
- [20] H. Moriwake, A. Kuwabara, C. A. J. Fisher, and Y. Ikuhara, Why is sodium-intercalated graphite unstable?, *RSC Adv.* 7 (2017) 36550.
- [21] Y. Liu, S. Wang, X. Sun, J. Zhang, F. uz Zaman, L. Hou, and C. Yuan, Sub-nanoscale engineering of MoO_2 clusters for enhanced sodium storage, *Energy & Environ Materials.* eem2. (2022) 12263.
- [22] G. Wang, S. Wang, X. Sun, Y. Liu, P. Nie, L. Hou, L. Chang, and C. Yuan, Metallic Mo_2C quantum dots confined in functional carbon nanofiber films toward efficient sodium storage: heterogeneous interface engineering and charge-storage mechanism, *ACS Appl. Energy Mater.* 5 (2022) 1114–1125.
- [23] P. Mudgal, H. Arora, J. Pati, M. K. Singh, M. Khetri, and R. S. Dhaka, Electrochemical performance of MoSeTe as anode for sodium ion batteries, *Proc. Indian Natl. Sci. Acad.* 88 (2022) 430–438.
- [24] M. Chandra, T. S. Khan, R. Shukla, A. Ahmed, A. Gupta, S. Basu, M. A. Haider, and R. S. Dhaka, Diffusion coefficient and electrochemical performance of NaVO_3 anode in Li/Na batteries. *Electrochimica Acta* 331C (2020) 135293.
- [25] E. Yang, H. Ji, and Y. Jung, Two-dimensional transition metal dichalcogenide monolayers as promising sodium ion battery anodes, *J. Phys. Chem. C.* 119 (2015) 26374.
- [26] P. Tao, J. He, T. Shen, Y. Hao, J. Yan, Z. Huang, X. Xu, M. Li, and Y. Chen, Nitrogen-doped MoS_2 foam for fast sodium ion storage, *Adv. Mater. Interfaces.* 6 (2019) 1900460.
- [27] S. Li, Y. Liu, X. Zhao, K. Cui, Q. Shen, P. Li, X. Qu, and L. Jiao, Molecular engineering on MoS_2 enables large interlayers and unlocked basal planes for high-performance aqueous Zn-ion storage, *Angew Chem Int Ed* 60 (2021) 20286.
- [28] S. Li, Y. Liu, X. Zhao, Q. Shen, W. Zhao, Q. Tan, N. Zhang, P. Li, L. Jiao, and X. Qu, Sandwich-like heterostructures of MoS_2 /graphene with enlarged interlayer spacing and enhanced hydrophilicity as high-performance cathodes for aqueous zinc-ion batteries, *Adv. Mater.* 33 (2021) 2007480.
- [29] L. David, R. Bhandavat, G. Singh, MoS_2 /graphene composite paper for sodium-ion battery electrodes, *ACS Nano.* 8 (2014) 1759–1770.
- [30] X. Wang, X. Shen, Z. Wang, R. Yu, and L. Chen, Atomic-scale clarification of structural transition of MoS_2 upon sodium intercalation, *ACS Nano.* 8 (2014) 11394–11400.
- [31] Y. Zhou, Y. Liu, M. Zhang, Q. Han, Y. Wang, X. Sun, X. Zhang, C. Dong, J. Sun, Z. Tang, F. Jiang, Rationally designed hierarchical N, P co-doped carbon connected 1T/2H- MoS_2 heterostructures with cooperative effect as ultrafast and durable anode materials for efficient sodium storage, *Chem. Eng. J.* 433 (2022) 133778.
- [32] H. Lim, S. Yu, W. Choi, and S. O. Kim, Hierarchically designed nitrogen-doped MoS_2 /silicon oxycarbide nanoscale heterostructure as high-performance sodium-ion battery anode, *ACS Nano.* 15 (2021) 7409–7420.
- [33] J. Wu, J. Liu, J. Cui, S. Yao, M. Ihsan-Ul-Haq, N. Mubarak, E. Quattrocchi, F. Ciucci, J.-K. Kim, Dual-phase MoS_2 as a high-performance sodium-ion battery anode, *J. Mater. Chem. A.* 8 (2020) 2114–2122.
- [34] P. Li, Y. Yang, S. Gong, F. Lv, W. Wang, Y. Li, M. Luo, Y. Xing, Q. Wang, and S. Guo, Co-doped 1T- MoS_2 nanosheets embedded in N, S-doped carbon nanobowls for high-rate and ultra-stable sodium-ion batteries, *Nano Res.* 12 (2019) 2218.
- [35] J. Wang, C. Luo, T. Gao, A. Langrock, A. C. Mignerey, and C. Wang, An advanced MoS_2 /carbon anode for high-performance sodium-ion batteries, *Small.* 11 (2015) 473–

48.

- [36] C. Lane, D. Cao, H. Li, Y. Jiao, B. Barbiellini, A. Bansil, and H. Zhu, Understanding phase stability of metallic 1T-MoS₂ anodes for sodium-ion batteries, *Condensed Matter*. 4 (2019) 53.
- [37] X. Geng, W. Sun, W. Wu, B. Chen, A. Al-Hilo, M. Benamara, H. Zhu, F. Watanabe, J. Cui, and T. Chen, Pure and stable metallic phase molybdenum disulfide nanosheets for hydrogen evolution reaction, *Nat. Commun.* 7 (2016) 10672.
- [38] M. Acerce, D. Voiry, and M. Chhowalla, Metallic 1T phase MoS₂ nanosheets as supercapacitor electrode materials, *Nature Nanotech.* 10 (2015) 313.
- [39] T. S. Sahu and S. Mitra, Exfoliated MoS₂ sheets and reduced graphene oxide-an excellent and fast anode for sodium-ion battery, *Sci. Rep.* 5 (2015) 12571.
- [40] C. Zhao, C. Yu, M. Zhang, Q. Sun, S. Li, M. Norouzi Bani, X. Han, Q. Dong, J. Yang, G. Wang, X. Sun, Enhanced sodium storage capability enabled by super wide-interlayer-spacing MoS₂ integrated on carbon fibers, *Nano Energy*. 41 (2017) 66–74.
- [41] C. Chen, G. Li, Y. Lu, J. Zhu, M. Jiang, Y. Hu, L. Cao, X. Zhang, Chemical vapor deposited MoS₂/electrospun carbon nanofiber composite as anode material for high-performance sodium-ion batteries, *Electrochim. Acta*. 222 (2016) 1751–1760.
- [42] T. S. Sahu, Q. Li, J. Wu, V. P. Dravid, S. Mitra, Exfoliated MoS₂ nanosheets confined in 3-D hierarchical carbon nanotube@graphene architecture with superior sodium-ion storage, *J. Mater. Chem. A*. 5 (2017) 355–363.
- [43] Z. Xu, X. Liu, K. Yao, Y. Ren, J. Li, X. Shen, and Z. Li, 1T MoS₂ growth from exfoliated MoS₂ nucleation as high rate anode for sodium storage, *Nanotechnology*. 33 (2022) 025602.
- [44] L. Ma, J. Wu, G. Zhu, Y. Lv, Y. Zhang, and H. Pang, Recent advances in two-dimensional materials for alkali metal anodes, *J. Mater. Chem. A*. 9 (2021) 5232.
- [45] L. Zeng, F. Luo, X. Xia, M. -Q. Yang, L. Xu, J. Wang, X. Feng, Q. Qian, M. Wei and Q. Chen, An Sn doped 1 H MoS₂ few-layer structure embedded in N/P co-doped bio-carbon for high performance sodium-ion batteries, *Chem. Commun.* 55 (2019) 3614.
- [46] A. Massaro, A. Pecoraro, A. B. Muñoz-García, and M. Pavone, First-Principles Study of Na Intercalation and Diffusion Mechanisms at 2D MoS₂ /Graphene Interfaces, *J. Phys. Chem. C*. 125 (2021) 2276.
- [47] H. Poh, F. Sanek, A. Ambrosi, G. Zhao, Z. Sofer, M. Pumera, Graphenes prepared by Staudenmaier, Hofmann and Hummers methods with consequent thermal exfoliation exhibit very different electrochemical properties, *Nanoscale*. 4 (2012) 3515–3522.
- [48] G. Kresse and J. Furthmüller, Efficient iterative schemes for ab initio total-energy calculations using a plane-wave basis set, *Phys. Rev. B*. 54 (1996) 11169.
- [49] P. E. Blöchl, Projector augmented-wave method, *Phys. Rev. B*. 50 (1994) 17953.
- [50] J. P. Perdew, K. Burke, and M. Ernzerhof, Generalized gradient approximation made simple, *Phys. Rev. Lett.* 77 (1996) 3865.
- [51] B. J. Berne, G. Ciccotti, and D. F. Coker, Classical and quantum dynamics in condensed phase simulations: Proceedings of the international school of physics, World Scientific. (1998).
- [52] G. Henkelman, B. P. Uberuaga, and H. Jónsson, A climbing image nudged elastic band method for finding saddle points and minimum energy paths, *J. Chem. Phys.* 113 (2000) 9901.
- [53] W. Su, P. Wang, Z. Cai, J. Yang, and X. Wang, One-pot hydrothermal synthesis of Al-doped MoS₂@graphene aerogel nanocomposite electrocatalysts for enhanced hydrogen evolution reaction, *Results Phys.* 12 (2019) 250–258.
- [54] Y. J. Tang, Y. Wang, X. L. Wang, S. L. Li, W. Huang, L. Z. Dong, C. H. Liu, Y. F. Li, Y. Q. Lan, Molybdenum disulfide/nitrogen-doped reduced graphene oxide nanocomposite with enlarged interlayer spacing for electrocatalytic hydrogen evolution, *Adv. Energy Mater.* 6 (2016) 1–7.
- [55] Y. Zhao, J. Tu, Y. Sun, X. Hu, J. Ning, W. Wang, F. Wang, Y. Xu, and L. He, Enhanced photocatalytic activity of 2H-MoSe₂ by 3d transition-metal doping, *J. Phys. Chem. C*. 122 (2018) 26570–26575.
- [56] D. Wang, Y. Xiao, X. Luo, Z. Wu, Y. J. Wang, and B. Fang, Swollen ammoniated MoS₂ with 1T/2H hybrid phases for high-rate electrochemical energy storage, *ACS*

- Sustain. Chem. Eng. 5 (2017) 2509.
- [57] W. J. Tang, X. L. Wang, D. Xie, X. H. Xia, C. D. Gu, and J. P. Tu, Hollow metallic 1T MoS₂ arrays grown on carbon cloth: A freestanding electrode for sodium ion batteries, *J. Mater. Chem. A* 6 (2018) 18318.
- [58] M. Wu, J. Zhan, K. Wu, Z. Li, L. Wang, B. Geng, L. Wang, D. Pan, Metallic 1T MoS₂ nanosheet arrays vertically grown on activated carbon fiber cloth for enhanced Li-ion storage performance, *J. Mater. Chem. A* 5 (2017) 14061.
- [59] Y. Huang, Y. Sun, X. Zheng, T. Aoki, B. Pattengale, J. Huang, X. He, W. Bian, S. Younan, N. Williams, J. Hu, J. Ge, N. Pu, X. Yan, X. Pan, L. Zhang, Y. Wei, J. Gu, Atomically engineering activation sites onto metallic 1T-MoS₂ catalysts for enhanced electrochemical hydrogen evolution, *Nat Commun.* 10 (2019) 982.
- [60] N. H. Attanayake, A. C. Thenuwara, A. Patra, Y. V. Aulin, T. M. Tran, H. Chakraborty, E. Borguet, M. L. Klein, J. P. Perdew, and D. R. Strongin, Effect of Intercalated Metals on the Electrocatalytic Activity of 1T-MoS₂ for the Hydrogen Evolution Reaction, *ACS Energy Lett.* 3 (2018) 7–13.
- [61] see Supplementary Information for more details.
- [62] X. Liu, L. Liu, Y. Wu, Y. Wang, J. Yang and Z. Wang, Rosette-like MoS₂ nanoflowers as highly active and stable electrodes for hydrogen evolution reactions and supercapacitors, *RSC Adv.* 9 (2019) 13820.
- [63] X. Geng, Y. Jiao, Y. Han, A. Mukhopadhyay, L. Yang, H. Zhu, Freestanding metallic 1T MoS₂ with dual ion diffusion paths as high rate anode for sodium-ion batteries, *Adv. Funct. Mater.* 27 (2017) 1702998.
- [64] Z. Li, K. Jiang, F. Khan, A. Goswami, J. Liu, A. Passian, and T. Thundat, Anomalous interfacial stress generation during sodium intercalation/extraction in MoS₂ thin-film anodes, *Sci. Adv.* 5 (2019) eaav2820.
- [65] S. Wang, F. Cao, Y. Li, Z. Zhang, D. Zhou, Y. Yang, and Z. Tang, MoS₂ -coupled carbon nanosheets encapsulated on sodium titanate nanowires as super-durable anode material for sodium-ion batteries, *Adv. Sci.* 6 (2019) 1900028.
- [66] G. Ali, A. Mehmood, H. Y. Ha, J. Kim, and K. Y. Chung, Reduced graphene oxide as a stable and high-capacity cathode material for Na-ion batteries, *Sci. Rep.* 7 (2017) 40910.
- [67] D. Hou, Dawei Xia, E. Gabriel, J. A. Russell, K. Graff, Y. Ren, C. -J. Sun, F. Lin, Y. Liu and H. Xiong, Spatial and temporal analysis of sodium-ion batteries, *ACS Energy Lett.* 6 (2021) 4023–4054.
- [68] Z. Hu, L. Wang, K. Zhang, J. Wang, F. Cheng, Z. Tao, and J. Chen, MoS₂ nanoflowers with expanded interlayers as high-performance anodes for sodium-ion batteries, *Angew. Chemie* 126 (2014) 13008.
- [69] Y. Xiao, Y. -F. Zhu, H. -R. Yao, P. -F. Wang, X. D. Zhang, H. Li, X. Yang, L. Gu, Y. -C. Li, T. Wang, Y. -X. Yin, X. -D. Guo, B. -H. Zhong, Y. -G. Guo, A stable layered oxide cathode material for high performance sodium-ion battery, *Adv. Energy Mater.* 9 (2019) 1803978.
- [70] J. Wang, J. Polleux, J. Lim, and B. Dunn, Pseudocapacitive contributions to electrochemical energy storage in TiO₂ (anatase) nanoparticles, *J. Phys. Chem. C* 111 (2007) 14925.
- [71] C. Choi, D. S. Ashby, D. M. Butts, R. H. DeBlock, Q. Wei, J. Lau and B. Dunn, Achieving high energy density and high power density with pseudocapacitive materials, *Nat. Rev. Mater.* 5 (2020) 5–19.
- [72] P. K. Dwivedi, S. K. Sapra, J. Pati, and R. S. Dhaka, Na₄Co₃(PO₄)₂P₂O₇/NC composite as a negative electrode for sodium-ion batteries, *ACS Appl. Energy Mater.* 4 (2021) 8076.
- [73] C. Chen, Y. Wen, X. Hu, X. Ji, M. Yan, L. Mai, P. Hu, B. Shan, and Y. Huang, Na⁺ intercalation pseudocapacitance in graphene-coupled titanium oxide enabling ultrafast sodium storage and long-term cycling, *Nat. Commun.* 6 (2015) 6929.
- [74] W. Choi, H. -C. Shin, J. M. Kim, J. -Y. Choi, and W. -S. Yoon, Modeling and applications of electrochemical impedance spectroscopy (EIS) for lithium-ion batteries, *J. Electrochem. Sci. Technol.* 11(1) (2020) 1–13.
- [75] Z. Chen, L. Cao, L. Chen, H. Zhou, K. Xie and Y. Kuang, Nanoplate-stacked baguette-like LiVO₃ as a high-performance cathode material for lithium-ion batteries, *J. Mater. Chem. A* 3 (2015) 8750–8755.
- [76] S. Chen, S. Huang, J. Hu, S. Fan, Y. Shang, M. E. Pam, X. Li, Y. Wang, T. Xu, Y. Shi, H. Y. Yang, Boosting sodium storage of Fe_{1-x}S/MoS₂ composite via het-

- erointerface engineering, *Nano-Micro Lett.* 11 (2019) 80.
- [77] D. Gui, Z. Wei, J. Chen, L. Yan, J. Li, P. Zhang, and C. Zhao, Boosting the sodium storage of the 1T/2H MoS₂@SnO₂ heterostructure via a fast surface redox reaction, *J. Mater. Chem. A* 9 (2021) 463.
- [78] L. Jing, G. Lian, J. Wang, M. Zhao, X. Liu, Q. Wang, D. Cui, and C. -P. Wong, Porous-hollow nanorods constructed from alternate intercalation of carbon and MoS₂ monolayers for lithium and sodium storage, *Nano Res.* 12(8) (2019) 1912–1920.
- [79] Y. Yu, G.-H. Nam, Q. He, X.-J. Wu, K. Zhang, Z. Yang, J. Chen, Q. Ma, M. Zhao, Z. Liu, F.-R. Ran, X. Wang, H. Li, X. Huang, B. Li, Q. Xiong, Q. Zhang, Z. Liu, L. Gu, Y. Du, W. Huang, H. Zhang, High phase-purity 1T'-MoS₂- and 1T'-MoSe₂-layered crystals, *Nature Chem.* 10 (2018) 638–643.
- [80] L. Zou, R. Qu, H. Gao, X. Guan, X. Qi, C. Liu, Z. Zhang, and X. Lei, MoS₂/RGO hybrids prepared by a hydrothermal route as a highly efficient catalytic for sonocatalytic degradation of methylene blue, *Results Phys.* 14 (2019) 102458.
- [81] L. Wu, X. Xu, Y. Zhao, K. Zhang, Y. Sun, T. Wang, Y. Wang, W. Zhong, and Y. Du, Mn doped MoS₂/reduced graphene oxide hybrid for enhanced hydrogen evolution, *Applied Surface Science* 425 (2017) 470.
- [82] D. M. Lutz, M. R. Dunkin, S. T. King, C. A. Stackhouse, J. Kuang, Y. Du, S. -M. Bak, D. C. Bock, X. Tong, L. Ma, S. N. Ehrlich, E. S. Takeuchi, K. J. Takeuchi, A. C. Marschilok, and L. Wang, Hybrid MoS_{2+x} nanosheet/nanocarbon heterostructures for lithium-ion batteries *ACS Appl. Nano Mater.* 5 (2022) 5103–5118.
- [83] Z. Lei, J. Zhan, L. Tang, Y. Zhang, and Y. Wang, Recent development of metallic (1T) phase of molybdenum disulfide for energy conversion and storage. *Adv. Energy Mater.* 8 (2018) 1703482.
- [84] M. Chhowalla, D. Voiry, J. Yang, H. S. Shin, and K. P. Loh, Phase-engineered transition-metal dichalcogenides for energy and electronics. *MRS Bull.* 40 (2015) 585–591.
- [85] Y. Zhu, H. Li, Y. Wu, L. Yang, Y. Sun, G. Chen, Y. Liu, Z. Wu, C. Zhang, X. Guo, Unveiling the abnormal capacity rising mechanism of MoS₂ anode during long-term cycling for sodium-ion batteries, *RSC Adv.* 11 (2021) 28488–28495.
- [86] Z. Li, X. Mu, Z. Zhao-Karger, T. Diemant, R. J. Behm, C. Kübel, and M. Fichtner, Fast kinetics of multivalent intercalation chemistry enabled by solvated magnesium-ions into self-established metallic layered materials, *Nat Commun.* 9 (2018) 5115.
- [87] Q. Huang, X. Li, M. Sun, L. Zhang, C. Song, L. Zhu, P. Chen, Z. Xu, W. Wang, and X. Bai, The mechanistic insights into the 2H–1T phase transition of MoS₂ upon alkali metal intercalation: from the study of dynamic sodiation processes of MoS₂ nanosheets, *Adv. Mater. Interfaces.* 4 (2017) 1700171.
- [88] F. Wypych and R. Schöllhorn, 1T–MoS₂, A new metallic modification of molybdenum disulfide, *J. Chem. Soc. Chem. Commun.* (1992) 1386.
- [89] V. Vandalon, A. A. Bol, M. A. Verheijen, W. M. M. Kessels, Atomic Layer Deposition of Al-Doped MoS₂: Synthesizing a p-Type 2D Semiconductor with Tunable Carrier Density, *ACS Appl. Nano Mater.* 3 (2020) 10200–10208.
- [90] R. Zhang, D. Fu, J. Ni, C. Sun, S. Song, Adsorption for SO₂ Gas Molecules on B, N, P and Al Doped MoS₂: The DFT Study, *Chem. Phys. Lett.* 715 (2019) 273–277.
- [91] H. Luo, Y. Cao, J. Zhou, J. Feng, J. Cao, H. Guo, Adsorption of NO₂, NH₃ on Monolayer MoS₂ Doped with Al, Si, and P: A First-Principles Study, *Chem. Phys. Lett.* 643 (2016) 27–33.
- [92] N. N. Hieu, H. V. Phuc, V. V. Ilyasov, N. D. Chien, N. A. Poklonski, N. Van Hieu, and C. V. Nguyen, First-principles study of the structural and electronic properties of graphene/MoS₂ interfaces, *J. Appl. Phys.* 122 (2017) 104301.
- [93] R. Kutner, Chemical diffusion in the lattice gas of non-interacting particles, *Phys. Lett. A* 81 (1981) 239.
- [94] D. Sun, D. Ye, P. Liu, Y. Tang, J. Guo, L. Wang, and H. Wang, MoS₂/graphene nanosheets from commercial bulky MoS₂ and graphite as anode materials for high rate sodium-ion batteries, *Adv. Energy Mater.* 8 (2018) 1.